

The resolved chemical composition of the starburst dwarf galaxy CGCG007-025: Direct method versus photoionization model fitting.

V. Fernández^{1,2*}, R. Amorín^{1,2}, R. Sanchez-Janssen³, M. G. del Valle-Espinosa⁴, P. Papaderos^{5,6}

¹Departamento de Astronomía, Universidad de La Serena, Av. Juan Cisternas 1200 Norte, La Serena, Chile

²Instituto de Investigación Multidisciplinar en Ciencia y Tecnología, Universidad de La Serena, Raúl Bitrán 1305, La Serena, Chile

³UK Astronomy Technology Centre, Royal Observatory, Blackford Hill, Edinburgh, EH9 3HJ, UK

⁴Institute for Astronomy, The University of Edinburgh, Royal Observatory, Blackford Hill, Edinburgh, EH9 3HJ, UK ⁵Centro de Astrofísica e Ciências do Espaço, Universi-

⁶Instituto de Astrofísica e Ciências do Espaço - Centro de Astrofísica da Universidade do Porto, Rua das Estrelas, 4150-762 Porto, Portugal

Accepted XXX. Received YYY; in original form ZZZ

ABSTRACT

This work focuses on the gas chemical composition of CGCG007-025. This compact dwarf is undergoing a galaxy wide star forming burst, whose spatial behaviour has been observed by VLT/MUSE. We present a new line measurement library to treat almost 7800 voxels. The direct method chemical analysis is limited to 484 voxels with good detection of the $[SIII]6312\text{\AA}$ temperature diagnostic line. The recombination fluxes are corrected for stellar absorption via a population synthesis. Additionally, we discuss a new algorithm to fit photoionization models via neural networks. The 8 ionic abundances analyzed show a spatial normal distribution with a $\sigma \sim 0.1\text{ dex}$, where only half this value can be explained by the uncertainty in the measurements. The oxygen abundance distribution is $12 + \log(O/H) = 7.88 \pm 0.11$. The $T_e[SIII]$ and $ne[SII]$ are also normally distributed. However, in the central and brightest region, the $ne[SII]$ is almost thrice the mean galaxy value. This is also reflected in the extinction measurements. The ionization parameter has a distribution of $\log(U) = -2.52^{0.17}_{0.19}$. The parameter spatial behaviour agrees with the S^{2+}/S^+ map. Finally, the discrepancies between the direct method and the photoionization model fitting are discussed. In the latter technique, we find that mixing lines with uneven uncertainty magnitudes can impact the accuracy of the results. In these fittings, we recommend overestimating the minimum flux uncertainty one order below the maximum line flux uncertainty. This provides a better match with the direct method.

Key words: galaxies:abundances – galaxies: dwarf – galaxies: evolution

1 INTRODUCTION

The astronomical community will remember 2022 for the successful deployment of the James Webb Space Telescope (see [Gardner et al. 2006](#)). Among the many breakthroughs achieved, the JWST early science observations of the SMACS J0723.3-7327 galaxy cluster produced over 30 publications in less than two months¹. Focusing on the data from the Near InfraRed Spectrograph (NIRSpec), five emission line galaxies were detected at $5.2 < z < 8.5$, (see [Carnall et al. 2022](#); [Schaerer et al. 2022](#); [Trump et al. 2022](#)). Despite the fact that this instrument flux calibration has yet to be evaluated (see [Birkmann et al. 2022](#)) numerous research groups are reaching similar conclusions: 1) The line flux ratios are in agreement with those observed in Extreme Emission Line Galaxies (EELG). This can be appreciated in the graphical comparisons by [Trump et al. \(2022\)](#) and [Brinchmann \(2022\)](#) with the SDSS samples of EELGs by [Pérez-Montero et al. \(2021\)](#) and [Izotov et al. \(2014\)](#) respectively. 2) The metallicities, derived via the direct method, thanks to the $[OIII]4363\text{\AA}$ auroral line detection, are around $\approx 0.1Z_{\odot}$ (see [Arellano-Córdova et al. 2022a](#); [Curti et al. 2022](#)). 3) The stellar mass tracers predict values within the $7.5 \lesssim \log(M_*) \lesssim 9.0$ range (see [Tacchella et al. 2022](#)). These

measurements lead to the following conclusion: There are still galaxies in the local universe with nebular properties closely resembling those in the 1 Gyr old universe.

This was already anticipated by, e.g., [Amorín et al. \(2010\)](#); [Schaerer et al. \(2016\)](#), while analysing the chemical content of Green Peas galaxies, in the local and (pre-JWST) high redshift universe (see [Amorín et al. 2012](#); [Schaerer et al. 2016](#); [Amorín et al. 2017](#)). Despite their compact sizes ($r_e < 5\text{ kpc}$) and low masses ($8.5 < \log(M_*) < 10$) (see [Cardamone et al. 2009](#)), these galaxies can be easily detected in spectroscopic surveys due to their intense nebular emission.

Moreover, since these emissions are likely constrained to a single filter, their vivid colors highlight them in photometric surveys. Beyond, the radiation from the stellar atmospheres, the main phenomenon dominating the emission properties is the gas composition. Indeed, at the optical range, the cooling of a low metallicity gas produces an enormous photons flux, from the forbidden transitions. Consequently, studying the chemistry of EELG not only improves our understanding on the local star formation phenomena, it can help us interpret the observations from the young universe.

In this manuscript, we present the initial results from an exhaustive analysis of the CGCG007-025 and UGC5205 galaxy pair. As mentioned by [van Zee \(2001\)](#), this isolated galaxy pair is very interesting. The authors stated that while the projected separation is 8.3 kpc (at

* E-mail: vital.fernandez@userena.cl

¹ ADS search including the body "SMACS 0723" and "JWST" keywords

a velocity difference of 84 km/s) there is a stark contrast between them: CGCG007-025 is undergoing a massive star formation phase, while UGC5205 is gas depleted. The observation of a tidal tail in UGC5205 encourages the idea that galactic interaction caused this state. CGCG007-025 is included in the COS Legacy Archive Spectroscopy Survey (CLASSY) (see [Berg et al. 2022](#)) for its high redshift analogue characteristics. Finally, this system proximity, $z \approx 0.047$, make it an ideal laboratory to study the spatial properties of star formation enhancing and quenching.

The current results focus on the gas chemical composition of CGCG007-025, *Catalogue of Galaxies and of Clusters of Galaxies* (see [Zwicky & Kowal 1968](#)). This galaxy cross-IDs include SDSS J094401.86-003832.1² from the *Space Digital Sky Survey* (see [Ahumada et al. 2020](#)), SHOC270 from the the *SDSS HII-galaxies with Oxygen abundances Catalog* (see [Kniazev et al. 2004](#)) and MCG +00-25-010 from the *Millennium Galaxy Catalogue* (see [Proprius et al. 2007](#)). The analysis is based on the Integrated Field Unit data cube from the MUSE (Multi Unit Spectroscopic Explorer) instrument (see [Bacon et al. 2010](#)). In addition to the chemical analysis, we take this opportunity to present novel techniques for the treatment of Big Data observations. Finally, the authors discuss the discrepancies between the direct method and the photoionization model fitting. Both analysis make use of a neural networks sampler to fit the observed fluxes. The conclusions reached provide useful guidelines in how to properly consider the flux, and its uncertainty, on Bayesian photoionization model fitting.

This manuscript has the following structure. Section 2 presents the observational data and the tools employed to analyse its continuum and emission features. Section 3 continues with the results from the direct method and photoionization modelling along with a brief methodology description. The discussion starts at section 4 interpreting CGCG007-025 physical properties. In section 4.1, we debate the impact on the methodology design on the photoionization modelling measurements. Finally, the main conclusions are summarized in section 5.

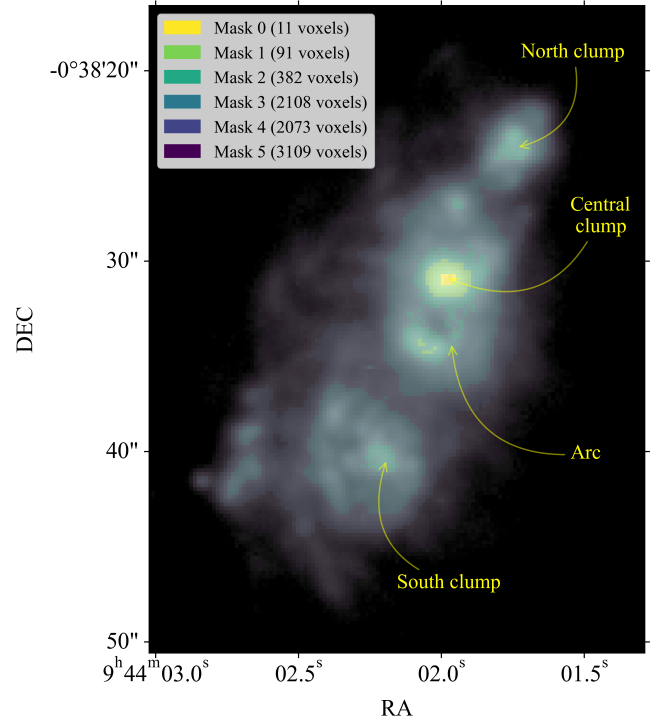


Figure 1. Continuum-subtracted $H\alpha$ map from the MUSE observation of CGCG007-025. The over-plotted shaded regions correspond to the spatial masks described in section 2.

2 OBSERVATIONAL DATA AND METHODOLOGY

The current analysis on CGCG007-025 is based on observations made with the ESO (European Southern Observatory) VLT (Very Large Telescope) facility at the La Silla Paranal Observatory under programme ID 0102.B-0325. The data cube was obtained the 27th of February 2019. The MUSE instrument wide field mode set up covered a 1 arcmin^2 field in a 316×328 voxel (volumetric pixel) array, where the $H\alpha$ emission extends over 7700 voxels. The SDSS observation of CGCG007-025 predicts a galactic redshift of $z = 0.00469$ resulting in a distance of 26.7 Mpc. This translates into a voxel spatial resolution around the 100 parsecs.

The data was downloaded from the ESO archive already reduced with the MUSE pipeline ([Weilbacher et al. 2012](#), version 1.2). The wavelength range is $4750 - 9349 \text{ \AA}$ with a constant spectral resolution of 1.25 \AA per pixel ($R_{H\alpha} = 5250$). The fits file is opened with the instrument MPDAF (Muse Python Data Analysis Framework) library by [Bacon et al. \(2016\)](#).

Several pixels in the $H\alpha$ band had non-a-numerical (NaN) value in the 5 most intense voxels of the central clump. Attempting to interpolate the missing entries resulted in relative $H\alpha$ fluxes, below the expected emissivity $H\alpha/H\beta = 2.86$ ratio. Moreover, in the central core of CGCG007-025 the $[OIII]5007\text{\AA}/[OIII]4959\text{\AA}$ flux ratio is below the theoretical emissivity ratio (≈ 2.97). This photons loss could be explained by the saturation of the CCD (Charge Coupled Device) or a loss in the CCD linearity due to the intense radiation from these transitions.

To deal with these issues, the cube voxels were labelled with a set of masks to tailor the chemical analysis for the available lines. These masks are over-plotted on the CGCG007-025 $H\alpha$ image in Fig.1. Regions 0, 1 and 2 correspond to the 99.99, 99.90 and 99.50

² The galaxy SDSS Plate-MJD-Fiber reference is 266-51630-100

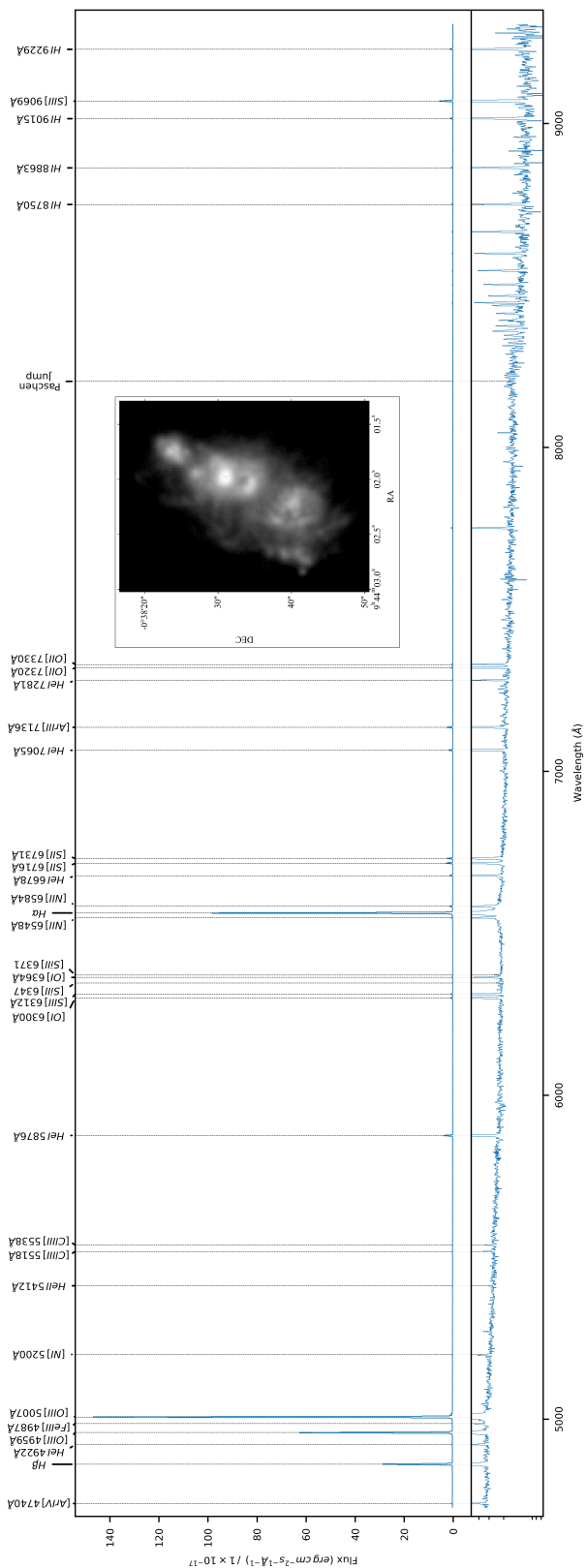


Figure 2. Spectrum from a voxel in the central core of CGCG007-025 with array coordinates 167-170. The lower panel is displayed in logarithmic scale with a constrained flux limits for a better focus on the continuum. The image corresponds to the $H\alpha$ band from the MUSE cube. The emission lines are labeled using the LINEIDPLOT library by [Nair \(2016\)](#)

Table 1. Emission line fluxes for the voxel 167-170 at the central CGCG007-025 cluster. Column (1) Wavelengths in Å at rest frame. The labels with a "g" subscript identify emission lines whose measurement consisted in a Gaussian profile deblending. The "w1", "w2" suffixes refer to additional kinematic components on the transitions. Column (2) Reddening curve. Columns (3-4) display the observed $F(\lambda)$ and extinction corrected $I(\lambda)$ fluxes relative to $F(H\beta) = I(H\beta) = 1000$. At the bottom of the table the logarithmic extinction coefficient, the equivalent width and the observed flux for $H\beta$ are tabulated (the flux units are $10^{-17} \text{ erg cm}^{-2} \text{ s}^{-1}$).

Line	f_l	$F(\lambda)$	$I(\lambda)$
4740Å [ArIV]	0.03	10 ± 1	10 ± 1
4861Å HI	0.00	1000 ± 4	1000 ± 4
4922Å HeI	-0.01	9 ± 1	8 ± 1
4959Å [OIII] _g	-0.02	1986 ± 48	1946 ± 47
4959Å [OIII] − w _{1g}	-0.02	35 ± 23	35 ± 23
4987Å [FeIII]	-0.03	5 ± 1	5 ± 1
5007Å [OIII] _g	-0.03	5542 ± 126	5377 ± 123
5007Å [OIII] − w _{1g}	-0.03	94 ± 25	91 ± 24
5016Å HeI _g	-0.04	19 ± 3	18 ± 3
5048Å HeI	-0.04	2 ± 1	2 ± 1
5192Å [ArIII]	-0.07	4 ± 1	4 ± 1
5272Å [FeIII]	-0.09	2 ± 1	2 ± 1
5412HeII	-0.12	1 ± 1	1 ± 1
5413Å [FeIII]	-0.12	1 ± 1	1 ± 1
5518Å [CIIII]	-0.14	3 ± 1	3 ± 1
5538Å [CIIII]	-0.14	2 ± 1	2 ± 1
5755Å [NII]	-0.18	1 ± 1	1 ± 1
5876Å HeI	-0.21	125 ± 1	103 ± 2
6300Å [OI]	-0.28	26 ± 1	20 ± 1
6312Å [SIII]	-0.28	19 ± 1	15 ± 1
6347 [SiII]	-0.29	1 ± 1	1 ± 1
6364Å [OI]	-0.29	8 ± 1	6 ± 1
6371 [SiII]	-0.29	1 ± 1	1 ± 1
6548Å [NII] _g	-0.32	13 ± 1	10 ± 1
6563Å HI − w _{1g}	-0.32	47 ± 7	36 ± 6
6563Å HI _g	-0.32	3582 ± 65	2680 ± 73
6584Å [NII] _g	-0.32	38 ± 1	29 ± 1
6678Å HeI	-0.34	40 ± 1	29 ± 1
6716Å [SII]	-0.34	83 ± 1	61 ± 1
6731Å [SII]	-0.34	68 ± 1	50 ± 1
7065Å HeI	-0.39	54 ± 1	38 ± 1
7136Å [ArIII]	-0.40	73 ± 1	51 ± 2
7170Å [ArIV]	-0.40	1 ± 1	1 ± 1
7281Å HeI	-0.41	8 ± 1	6 ± 1
7319Å [OII]	-0.42	21 ± 1	14 ± 1
7330Å [OII]	-0.42	17 ± 1	12 ± 1
7530Å [CIIV]	-0.44	1 ± 1	1 ± 1
7751Å [ArIII]	-0.47	18 ± 1	12 ± 1
8045Å [CIIV]	-0.50	2 ± 1	1 ± 1
8359Å HI	-0.53	5 ± 1	3 ± 1
8374Å HI	-0.53	2 ± 1	1 ± 1
8446Å HeI	-0.53	10 ± 1	6 ± 1
8467Å HI	-0.54	7 ± 1	4 ± 1
8545Å HI	-0.54	9 ± 1	6 ± 1
8665Å HI	-0.55	13 ± 1	8 ± 1
8750Å HI	-0.56	18 ± 1	11 ± 1
8863Å HI	-0.57	23 ± 1	14 ± 1
9015Å HI	-0.58	33 ± 1	20 ± 1
9069Å [SIII]	-0.59	180 ± 2	106 ± 4
$c(H\beta)$		0.39 ± 0.03	
−W(β) (Å)		280 ± 21	
F(Hβ)		89 ± 1	

flux percentiles of the $[SIII]6312\text{\AA}$ band, our temperature diagnostic transition. Region 0 has the 11 most intense emission voxels, including those with the $H\alpha$ NaN pixels. Region 1 covers 91 voxels, where the O^{2+} lines flux ratio is below the expected theoretical value. Finally, region 2 covers the remaining 382 voxels where the $[SIII]6312\text{\AA}$ has a good S/N ratio for a direct method analysis. Region 4, 5 and 6 correspond to the 97.50, 95.50 92.50 flux percentiles of the $H\alpha$ band. These regions have 2108, 2073 and 3109 voxels respectively.

2.1 Emission line measurement

The emission flux measurements and the Gaussian profile fittings were computed with LiME, the LIne MEasuring library (Fernández et al, in prep). This python-based package has been developed by the authors for the analysis of large spectra samples with complex line profiles. Since this work represents its beta release³, the following paragraphs describe its workflow:

(i) The user introduces a line spectral masks list. This is a 7 column table text file. The first column contains the line label (i.e. $H1_{6563A}$). The remaining columns provide the wavelength values (in the rest frame), which are used to index the line location and two adjacent continua bands. These wavelengths are sorted from lower to higher wavelength values. This design adheres to the Lick indexes (see Worthey 1994) for the analysis of stellar spectra. As we move to regions with lower ionization, the input masks exclude weaker emission lines in order to avoid false detections in noisier spectra.

(ii) The galaxy continuum is fitted in an iterative process with a polynomial function. At each step, pixels deviating from the fit (including those in emission/absorption lines) are excluded to better characterise the object continuum. This calculation takes into account the pixel uncertainty if provided by the user. The output polynomial is used to normalise the input spectrum. This baseline is introduced in a peak detection algorithm (see Yang et al. 2009) from the SciPy library by Virtanen et al. (2020). This provides the flux peaks and/or troughs pixels on the spectrum. In this work, the detection threshold was 3 times the normalized flux uncertainty for the emission lines and 2 for the absorptions lines.

(iii) The algorithm compares the input mask line regions with the peak/trough indexes found on the voxel spectrum (taking into consideration the galaxy redshift). In those cases with a match, a positive detection is assumed. For single lines, the algorithm adjusts the line mask to the FWZI (Full Width Zero Intensity) using the adjacent continua bands to compute the line continuum.

(iv) Among other parameters, each detected line has two flux calculations: The first one consists in one thousand loop Monte Carlo integration, while the second is a single/multi-Gaussian profile fitting. In both computations, the algorithm includes the sigma uncertainty spectrum from the current voxel to propagate the error into the measurements. For the chemical analysis, the integrated flux is used for single lines while for blended lines the Gaussian flux is used.

(v) The profile fitting is handled by the LMFit library by Newville et al. (2014). Our algorithm, however, does not use the default Gaussian parametrisation in LMFit. Instead, we define a model where A_i is the Gaussian peak height (with respect to the line continuum), μ_i is the peak central wavelength and σ_i is the Gaussian curve standard deviation. The subscript i corresponds to the Gaussian com-

ponent index. This flux is computed from the theoretical relation $(A_i \cdot \sqrt{2\pi} \cdot \sigma_i)$.

(vi) The library allows the user to define many constraints for the analysis of multiple kinematic components. However, in this observation of CGCC007-025 the only blended lines were a wide component in $H\beta$, $[OIII]4959\text{\AA}$, $[OIII]5007\text{\AA}$ and two in $H\alpha$, at the central clump. In the region 2 voxels, no wide components are observed and every line is assumed to have a single kinematic component.

The LiME script took 93 minutes to measure almost 61800 lines in the masked 7774 voxels (in a 3.6-GHz AMD-Ryzen7-3700X desktop). In the central clump of CGCC007-025, up to 45 lines are measured per voxel. This is the case of the voxel spectrum in Fig.2 corresponding to the central core of region 0. Table 1 shows the line fluxes and extinction corrected intensities for the same voxel. In contrast, most of the voxels in regions 3, 4 and 5 only display 4 lines. The line measurements are stored as tables in a fits file, using the voxel coordinates (from the cube rectangular array) to label each extension. This file has a 18 MB compressed size and it is available on the manuscript online support material. The reader is encouraged to check the LiME documentation at [lime-stable.readthedocs](https://lime-stable.readthedocs.io) regarding the physical/mathematical description of these measurements.

2.2 Stellar population synthesis

The stellar population synthesis on CGCG007-025 continuum was done with FADO by Gomes & Papaderos (2017) and PORTO3D by Papaderos et al. (2013); Gomes et al. (2016) which invokes the population synthesis code STARLIGHT by Fernandes et al. (2005). The Simple Stellar Population (SSP) library uses the Chabrier (2003) Initial Mass Function (IMF) with the Padova 1994 tracks (see Gustavo 2001). This treatment takes into consideration the nebular continuum in those voxels with a very young star forming region. This is computed from the intensity of the emission features. A very similar analysis was performed in Fernández et al. (2021) for the analysis of long-slit spectra of Green Pea galaxies. This work compared the nebular continua computed by FADO with an iterative calculation of the nebular continuum taking consideration the gas chemistry. Both techniques produced consistent results. A future manuscript, (Sánchez-Janssen et al, in preparation) will focus on the star formation history of CGCG007-025 and discuss the implications from these measurements. In the current work, however, these fittings are just used to measure the absorption from the underlying stellar population. This is done to better characterise the extinction from the hydrogen lines and the abundance from the helium transitions. The absorption lines measurements was done using LiME. The workflow is very similar to the steps in section 2.1.

The $H\alpha$ and $H\beta$ absorption lines can be measured in the complete galaxy. However, the remaining H I and He I lines are either too weak or non-detected in a large fraction of the voxels. Even in the low ionization regions, the emission component is at least one order of magnitude above the absorptions fluxes. The relative absorption of the recombination features, with respect to $H\beta$, shows a normal distribution for all the lines and all the spatial masks. Table 2 shows the mean and standard deviation for the hydrogen and helium lines relative to the $H\beta$. The number of voxels used to calculate each value is displayed in the third column. These constraints lead to the following strategy in the extinction and chemical analysis: In the case of $H\alpha$ and $H\beta$, the emission fluxes are corrected by the absorption flux measured at each voxel. For the remaining lines, we use the

³ The library documentation and resources can be found at <https://lime-stable.readthedocs.io>

Table 2. CGCG007-025 mean absorption intensity relative to $H\beta$. Each transition includes the number of voxels where the absorption line was detected in the fittings of the stellar populations synthesis.

Line	Relative absorption	Voxels
4861Å $H\text{I}$	1.0	7419
4922Å $He\text{I}$	0.10 ± 0.03	528
5016Å $He\text{I}$	0.06 ± 0.02	879
5876Å $He\text{I}$	0.05 ± 0.02	253
6563Å $H\text{I}$	0.49 ± 0.22	7364
6678Å $He\text{I}$	0.05 ± 0.01	48
8750Å $H\text{I}$	0.08 ± 0.03	229
8863Å $H\text{I}$	0.10 ± 0.03	506
9015Å $H\text{I}$	0.02 ± 0.02	708
9229Å $H\text{I}$	0.04 ± 0.02	549

averaged values from Table 2. In both scenarios, we propagate the error into the emission line flux.

3 ANALYSIS AND RESULTS

In the previous section, we described how there are drops on the $[OIII]5007\text{\AA}$ and $H\alpha$ fluxes in regions 0 and 1. For security's sake, both lines are excluded from the chemical analysis of the 102 voxels covered in these spatial masks. In the calculations, where the $[OIII]5007\text{\AA}$ flux is necessary, the value used is $2.97 \cdot [OIII]4959\text{\AA}$. Similarly, instead of using the $H\alpha$ flux in the logarithmic extinction coefficient calculation, we use $H\beta$ and the brightest Paschen lines in our wavelength range: HI_{P12} 8750Å, HI_{P11} 8863Å, HI_{P10} 9015Å and HI_{P9} 9229Å. The spatial plots of these lines fluxes (normalized by $H\beta$) shows a consisting pattern with higher ratios at the central core of CGCG007-025. This can be appreciated in Fig.3. In region 2, both $H\alpha$ and $[OIII]5007\text{\AA}$ are included in the analysis while the Paschen lines are excluded due to their low signal-to-noise ratio.

Table A1 at the appendix includes the references for the ionic species measured in this study. The transitions emissivity are calculated using PyNEB by Luridiana et al. (2015). The following subsections provide a brief recap of the methodologies employed as well as the tabulated results. The data corresponding to individual voxels can be found on the online support material.

3.1 Extinction

The average Large Magellanic Cloud (LMC) reddening law by Gordon et al. (2003) was selected for this study, assuming $R_V = 3.1$. This curve was deemed appropriate for a very young star forming region. The hydrogen emissivities are calculated assuming a uniform spatial temperature and density of 10000 K and 100 cm^{-3} respectively.

The mean voxel extinction of CGCG007-025 presents a low dust content with $cH(\beta) = 0.11 \pm 0.11$. However, the core clump has a distinctive higher value. Fig.4 displays the $cH(\beta)$ histogram, color-coded according to the galaxy spatial masks. The brightest 11 voxels show a tight mean value of $cH(\beta) = 0.50 \pm 0.06$ which drops to $cH(\beta) = 0.22 \pm 0.09$ for the 91 voxels in region 1. In the outer regions of CGCG007-025, we start to see some negative values of $cH(\beta)$. This can be explained by the low degree of ionisation: As $H\alpha$ and $H\beta$ become weaker, the observational noise affects the quality of the line flux measurement. Moreover, in the outskirts, the strength of the underlying stellar population absorption starts to be of the same order as the gas emission. This makes the accuracy of this correction more critical. These two parameters contribute to a poor

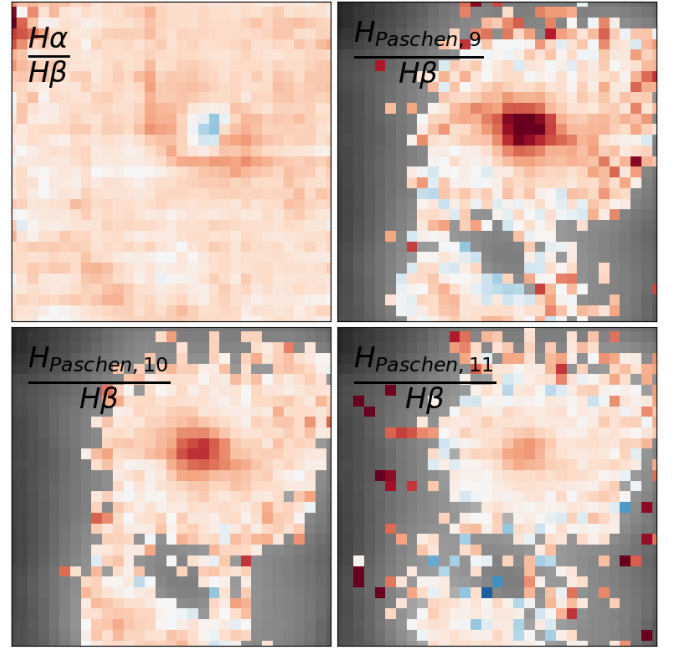


Figure 3. Hydrogen line fluxes relative to $H\beta$ over the central cluster of CGCG007-025. The voxels with successful line detection are color coded: White voxels are close to the theoretical emissivity ratio, while red/blue voxels are above/below respectively. The drop in $H\alpha$ flux at the galaxy core is due to non-numeric pixels at the line. The background grey-scale voxels correspond to the $H\alpha$ band.

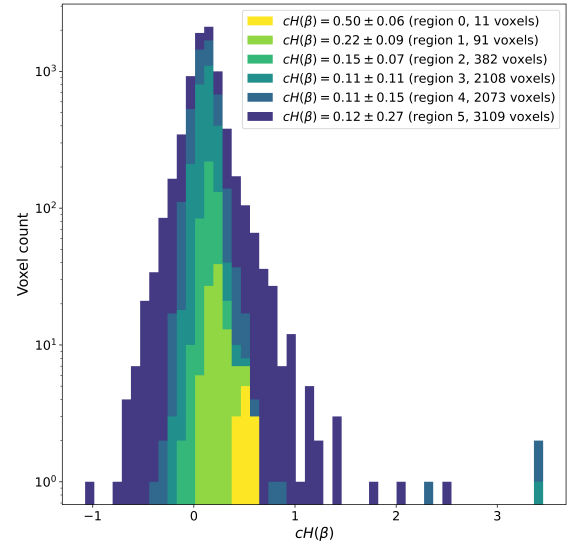


Figure 4. Logarithmic stacked histogram with the voxel logarithmic extinction coefficient, $cH(\beta)$ spatial distribution. The histogram is color coded according to the spatial mask region. The legend includes the number of voxels at each spatial mask alongside the mean $cH(\beta)$ from the region voxels

linear regression on the $cH(\beta)$ calculation. Despite this, even in region 5, the extinction coefficient distribution is still centered at $cH(\beta) = 0.12 \pm 0.27$.

3.2 Direct method physical properties

The direct method is an observation-based treatment, where the ionic abundances are calculated directly from the observed fluxes. This approach assumes some simplifications on the ionization structure to characterise the electron temperature (T_e) and density (n_e). These parameters can be measured from the photons flux ratio of transitions, which are sensitive to them. However, these auroral lines are very weak. Consequently, this methodology usually imposes a hard constraint on the object selection due to the signal-to-noise requirement. In the case of CGCG007-025, the direct method is limited to 484 pixels from regions 0, 1 and 2.

In [Fernández et al. \(2019\)](#), the authors presented a novel approach to fit the complete direct method parameter space simultaneously. This model consisted in one electron density, two electron temperatures, the logarithmic extinction coefficient, the optical depth for the HeI transitions and nine ionic species. An important advantage of this methodology was a more robust error propagation for the parameters, as well as, a faster treatment. The following paragraphs provide a brief summary:

- The ionic transitions emissivities are interpolated at every step as a function of the sampled temperature and density by the *RegularGridInterpolator* function from the *EXOPLANET* library by [Foreman-Mackey et al. \(2021\)](#).

- The solution sampling follows a Bayesian paradigm, where the prior distributions can be found in Table A2. The posterior solution is explored by a No-U-Turns (NUTs) sampler from the PyMC3 library by [Salvatier et al. \(2016\)](#). The likelihood is defined with a Gaussian distribution for each line. These distributions standard deviation is the uncertainty of the emission line fluxes. Consequently, lines with higher error result in wider likelihoods, assigning flatter probabilities to the parameters involved on line flux. The likelihoods center is computed from the theoretical fluxes at the sampled coordinate using the relation:

$$\frac{F_{X^{i+}, \lambda}}{F_{H\beta}} = X^{i+} \frac{\epsilon_{X^{i+}, \lambda}(T_e, n_e)}{\epsilon_{H\beta}(T_e, n_e)} \cdot 10^{-c(H\beta) \cdot f_\lambda} \quad (1)$$

where $\epsilon_{X^{i+}, \lambda}/\epsilon_{H\beta}$ is the relative emissivity at the transition wavelength λ , for an ion with abundance X^{i+} , for an electron density n_e and temperature T_e (K). $c(H\beta)$ is the logarithmic extinction coefficient at $H\beta$ and f_λ is the reddening curve.

- A common electron density is assumed for all the species. This parameter is anchored by the S^+ emission from the $[SII]6716, 6731\text{\AA}$ doublet.

- The chemical model considers two electron temperatures for a low and high ionization region, T_{low} and T_{high} respectively. In the high ionization region the Ar^{3+} , O^{2+} and y^+ ions are located, while the remaining species belong to the low ionization region. The low ionization temperature is derived from the from the $[SIII]6312\text{\AA}$ auroral line. Even though, the S^{2+} belongs to a midway ionization regime, the fast transition in the S^+ and S^{2+} fractions, makes this a reasonable assumption (see [Fernández 2018, Fig.4](#)) In our observation wavelength range, there are not suitable diagnostics for the high ionisation temperature. As a proxy, we are using the empirical relation from [Hägele et al. \(2006\)](#) to determine the O^{2+} temperature:

$$T_{high} = T_{[OIII]} = 0.8403 \cdot T_{[SIII]} + 2689 \text{ (K)} \quad (2)$$

The final model consists in 11 dimensions: n_e , T_{low} , $c(H\beta)$ and eight ionic species (Ar^{2+} , Ar^{3+} , N^+ , O^+ , O^{2+} , S^+ , S^{2+} and y^+). It needs to be emphasized that even though our model considers two ionic temperatures, T_{high} is not a free parameter. Indeed, due to the available lines, only T_{low} can be measured from the observed data, while T_{high} is computed from eq.2 at each sampling step. Consequently, the model outputs do not include a T_{high} distribution.

3.2.1 Electron densities, temperatures and $c(H\beta)$ distributions

Table 3 displays the $c(H\beta)$ coefficient, the electron temperatures and densities from the direct method fitting using the neural networks sampler. The first column corresponds to the distribution from all the voxels, while the subsequent columns are limited to the spatial masks displayed in Fig 1 and described in section 2.

The logarithmic extinction coefficients seem to be slightly higher than those from those linear regression on hydrogen recombination coefficients. However, these small discrepancies are within the measurement uncertainty for all the regions considered. The deviation can be explained by the different model: In the extinction linear regression the emissivities are calculated using constant $T_e = 10000 \text{ K}$ and $n_e = 100 \text{ cm}^{-3}$ values. In contrast, the direct method fits all the parameters simultaneously, included the temperature and density. In [Fernández et al. \(2019\)](#), we argued that the slightly higher uncertainty for extinction coefficients from this approach could be due to an uneven spatial dust distribution: While the hydrogen lines cover a very wide volume, the metals emission is expected to be closer to the new born stars. If the latter region has different dust properties, including the metals emission could bring a bias. However, as we can see from this spatial study, the $c(H\beta)$ values from both techniques have consistent nominal values and uncertainties.

The low ionization temperature of CGCG007-025 is $T_{low} = 14776 \pm 1336 \text{ K}$. This temperature distribution profile is Gaussian-like for all the regions and the increase in uncertainty as we move towards the outskirts of CGCG007-025 clusters can be explained by the larger uncertainty in the $[SIII]6312\text{\AA}$ flux measurement. The high ionization temperature for CGCG007-025 derived from eq.2 is $T_{high} = 15105 \pm 1122 \text{ K}$. At this regime, there is a high linearity between the O^{2+} and S^{2+} temperatures (see [Garnett 1992; Hägele et al. 2006; Pérez-Montero 2014; Fernández 2018](#)). Our model, however, does not take into consideration the uncertainty on the linear relation coefficients.

Overall, the electron density derived from the S^+ doublet remains uniform across the brightest clusters of CGCG007-025. The mean density from the 484 voxels is $n_e = 107_{47}^{84} \text{ cm}^{-3}$. This is the canonical value for the gas in low metallicity star forming regions as there is a well, on the photoionization equilibrium (see [Osterbrock 1974](#)). However, there is a significant density rise at the central, brightest cluster of the galaxy with a $n_e = 378_{63}^{34} \text{ cm}^{-3}$ distribution. This density decreases to $n_e = 177_{64}^{84} \text{ cm}^{-3}$ for region 1.

3.2.2 Ionic and total abundances

The ionic abundance distributions are tabulated in Table 3 for the different regions considered. The higher abundance uncertainty in region 2 can be explained by larger error on the temperature determination as the auroral line has a lower signal-to-noise at the clusters edge. This can be appreciated from the values in brackets which correspond to the mean parameter uncertainty for the considered voxels. Thus the width on the ionic abundances distribution can be partially

Table 3. CGCG007-025 chemical properties from the neural direct method fitting. The columns corresponds to results from all, region 0, region 1 and region 2 voxels respectively. The tabulated values represent the median measurements distribution and the 16th-84th percentiles. The values in brackets correspond to the mean parameter uncertainty in the measurements. The chemical model computes the high ionization temperature ($T_{high} = T_{[OIII]}$) using eq.2. The metal abundances in the 12 + log (X/H) scale.

Parameter	All voxels	Mask 0 (11 voxels)	Mask 1 (91 voxels)	Mask 2 (382 voxels)
$n_e (cm^{-3})$	104.0 ^{84.0} _{47.0} (51.0)	378.0 ^{34.0} _{63.0} (63.0)	177.0 ^{84.0} _{64.0} (53.0)	91.0 ^{59.0} _{38.0} (49.0)
$T_{low} (K)$	14776.0 ^{1322.0} _{1345.0} (870.0)	14802.0 ^{204.0} _{169.0} (281.0)	15030.0 ^{1192.0} _{643.0} (440.0)	14577.0 ^{1527.0} _{1361.0} (979.0)
$c(H\beta)$	0.21 ^{0.08} _{0.08} (0.02)	0.54 ^{0.06} _{0.04} (0.01)	0.27 ^{0.07} _{0.08} (0.01)	0.19 ^{0.07} _{0.07} (0.02)
Ar^{3+}/H^+	4.91 ^{0.17} _{0.26} (0.13)	5.06 ^{0.01} _{0.04} (0.03)	4.92 ^{0.11} _{0.16} (0.06)	4.87 ^{0.25} _{0.31} (0.17)
Ar^{2+}/H^+	5.27 ^{0.08} _{0.08} (0.05)	5.25 ^{0.02} _{0.04} (0.02)	5.27 ^{0.04} _{0.09} (0.03)	5.27 ^{0.1} _{0.09} (0.06)
O^+/H^+	7.36 ^{0.22} _{0.2} (0.12)	7.18 ^{0.04} _{0.03} (0.04)	7.20 ^{0.14} _{0.09} (0.06)	7.43 ^{0.19} _{0.23} (0.14)
O^{2+}/H^+	7.71 ^{0.09} _{0.11} (0.06)	7.79 ^{0.02} _{0.01} (0.02)	7.74 ^{0.05} _{0.09} (0.03)	7.70 ^{0.1} _{0.11} (0.06)
N^+/H^+	5.53 ^{0.14} _{0.14} (0.06)	5.33 ^{0.02} _{0.02} (0.03)	5.40 ^{0.1} _{0.05} (0.03)	5.57 ^{0.12} _{0.14} (0.06)
y^+	0.076 ^{0.004} _{0.004} (0.003)	0.071 ^{0.001} _{0.001} (0.001)	0.076 ^{0.003} _{0.002} (0.002)	0.077 ^{0.004} _{0.004} (0.003)
S^+/H^+	5.26 ^{0.15} _{0.15} (0.05)	5.03 ^{0.03} _{0.01} (0.02)	5.13 ^{0.1} _{0.05} (0.02)	5.3 ^{0.12} _{0.13} (0.06)
S^{2+}/H^+	5.91 ^{0.09} _{0.08} (0.05)	5.88 ^{0.02} _{0.02} (0.02)	5.90 ^{0.04} _{0.07} (0.03)	5.92 ^{0.1} _{0.09} (0.06)

Table 4. Chemical spatial distributions for the methodologies discussed in the text. The first row contains the elemental abundances from the direct method. The following columns contain the measurements for the 12 + log (O/H) abundance, the N/O excess and the ionization parameter log(U) for the Photoionization model fitting techniques. The columns corresponds to results from the total, region 0, region 1 and region 2 voxels respectively. The tabulated values represent the median measurements distribution and the 16th-84th percentiles.

Methodology	Parameter	All voxels	Region 0 (11 voxels)	Region 1 (91 voxels)	Region 2 (382 voxels)
Direct method	O	7.88 ^{0.11} _{0.11}	7.88 ^{0.03} _{0.01}	7.87 ^{0.05} _{0.09}	7.88 ^{0.12} _{0.12}
	N	-1.85 ^{0.12} _{0.12}	-1.85 ^{0.02} _{0.02}	-1.81 ^{0.08} _{0.07}	-1.85 ^{0.13} _{0.14}
	O/N	6.04 ^{0.06} _{0.06}	6.03 ^{0.02} _{0.01}	6.05 ^{0.03} _{0.05}	6.03 ^{0.07} _{0.06}
	Ar	5.43 ^{0.08} _{0.11}	5.46 ^{0.02} _{0.02}	5.43 ^{0.05} _{0.11}	5.43 ^{0.11} _{0.11}
	H	6.15 ^{0.1} _{0.09}	6.15 ^{0.02} _{0.01}	6.14 ^{0.05} _{0.08}	6.16 ^{0.11} _{0.11}
	ICF(S ³⁺)	1.47 ^{0.19} _{0.22}	1.66 ^{0.07} _{0.08}	1.48 ^{0.12} _{0.1}	1.42 ^{0.24} _{0.2}
	S	-1.73 ^{0.08} _{0.07}	-1.73 ^{0.02} _{0.02}	-1.72 ^{0.03} _{0.03}	-1.73 ^{0.09} _{0.09}
	O	7.97 ^{0.05} _{0.14}	7.73 ^{0.01} _{0.0}	7.94 ^{0.05} _{0.19}	7.98 ^{0.04} _{0.11}
	N	-1.47 ^{0.03} _{0.04}	-1.44 ^{0.02} _{0.0}	-1.46 ^{0.02} _{0.02}	-1.48 ^{0.04} _{0.04}
	log(U)	-2.44 ^{0.17} _{0.14}	-2.14 ^{0.06} _{0.04}	-2.28 ^{0.06} _{0.1}	-2.47 ^{0.13} _{0.12}
HII-CHI-MISTRY	O	7.94 ^{0.05} _{0.08}	7.88 ^{0.03} _{0.04}	7.93 ^{0.05} _{0.06}	7.94 ^{0.05} _{0.06}
	N	-1.39 ^{0.04} _{0.04}	-1.38 ^{0.02} _{0.02}	-1.4 ^{0.03} _{0.02}	-1.39 ^{0.05} _{0.05}
	O	-2.49 ^{0.15} _{0.17}	-2.22 ^{0.09} _{0.12}	-2.39 ^{0.12} _{0.11}	-2.53 ^{0.14} _{0.16}
	log(U)	-2.49 ^{0.15} _{0.17}	-2.22 ^{0.09} _{0.12}	-2.39 ^{0.12} _{0.11}	-2.53 ^{0.14} _{0.16}
Neural model fitting (observed line fluxes and uncertainty)	O	7.96 ^{0.05} _{0.04}	7.92 ^{0.02} _{0.02}	7.95 ^{0.03} _{0.03}	7.97 ^{0.04} _{0.06}
	N	-1.37 ^{0.05} _{0.04}	-1.3 ^{0.02} _{0.01}	-1.34 ^{0.03} _{0.03}	-1.39 ^{0.04} _{0.04}
	O	-2.4 ^{0.2} _{0.23}	-2.04 ^{0.03} _{0.06}	-2.25 ^{0.14} _{0.14}	-2.47 ^{0.15} _{0.15}
	log(U)	-2.4 ^{0.2} _{0.23}	-2.04 ^{0.03} _{0.06}	-2.25 ^{0.14} _{0.14}	-2.47 ^{0.15} _{0.15}
Neural model fitting (same HII-CHI-mistry inputs)	O	7.95 ^{0.09} _{0.08}	7.91 ^{0.02} _{0.0}	7.94 ^{0.06} _{0.03}	7.97 ^{0.08} _{0.1}
	N	-1.33 ^{0.08} _{0.15}	-1.34 ^{0.02} _{0.02}	-1.33 ^{0.02} _{0.03}	-1.33 ^{0.1} _{0.17}
	O	-2.3 ^{0.13} _{0.47}	-2.12 ^{0.02} _{0.03}	-2.25 ^{0.1} _{0.1}	-2.33 ^{0.14} _{0.5}
	log(U)	-2.3 ^{0.13} _{0.47}	-2.12 ^{0.02} _{0.03}	-2.25 ^{0.1} _{0.1}	-2.33 ^{0.14} _{0.5}
Neural model fitting (Uniform maximum observed uncertainty)	O	7.91 ^{0.07} _{0.06}	7.88 ^{0.03} _{0.04}	7.92 ^{0.05} _{0.06}	7.91 ^{0.08} _{0.06}
	N	-1.4 ^{0.05} _{0.05}	-1.38 ^{0.02} _{0.02}	-1.4 ^{0.05} _{0.05}	-1.4 ^{0.05} _{0.06}
	O	-2.5 ^{0.17} _{0.19}	-2.22 ^{0.09} _{0.12}	-2.39 ^{0.12} _{0.12}	-2.57 ^{0.17} _{0.16}
	log(U)	-2.5 ^{0.17} _{0.19}	-2.22 ^{0.09} _{0.12}	-2.39 ^{0.12} _{0.12}	-2.57 ^{0.17} _{0.16}

explained by the bias on the measurement precision rather than the existence of several chemical components.

In the case of oxygen, the total abundance can be computed directly from the O^+ and O^{2+} abundances as these ions are the main components (see Pagel et al. 1978). For the sulfur abundance, the ionization potential of S^{3+} is sufficiently low for a non negligible component at the hottest gas of the galaxy (see Oey & Shields 2000). To account for this contribution, we use the ionization correction factor, $ICF(S^{3+})$ presented in Fernández et al. (2018):

$$\log \left(\frac{Ar^{2+}}{Ar^{3+}} \right) = a \cdot \log \left(\frac{S^{2+}}{S^{3+}} \right) + b \quad (3)$$

where $a = 1.162 \pm 0.006$ and $b = 0.05 \pm 0.01$. In those voxels, where the weak $[ArIV]4740\text{\AA}$ line is not detected, it is assumed that the S^{3+} fraction is negligible.

For the nitrogen abundance calculation, we take the approximation

that the N^+/O^+ ratio equals the N/O ratio in the low metallicity regime (see Garnett 1990). Consequently, the nitrogen abundance is the result of multiplying this ratio by the oxygen abundance.

Due to the high ionization potential of He^+ , the y^{2+} abundance is very small and dominated by phenomena beyond the photoionization of stellar atmospheres. In Fernández (2018) low metallicity HII galaxy sample, the y^{2+}/y^+ ratio was always below 3%. In our wavelength range, we do not have access to the $HeII4865\text{\AA}$ transition. However, at central region of CGCG007-025, it may be possible to distinguish the $HeII5412\text{\AA}$ emission from the 4-7 Pickering series. Computing the abundance from its flux (Table 1) using T_{high} , the relative ionic fraction is $y^{2+}/y^+ \lesssim 0.99$. A similar regime has been reported in the primordial helium galaxy sample by Peimbert et al. (2016). Regarding, the neutral helium fraction, Pagel et al. (1992) argued that at the intense radiation fields encountered in low metal-

licity BCD, the neutral fraction is very small. The models presented by the authors stated that the $ICF(He) \approx 1$ for $\eta < 0.9$. As it will be discussed in 4.1 this is the case of CGCG007-025. Consequently, it is reasonable to assume that $y \approx y^+$.

Finally, the argon abundance can be characterised by the sum of the Ar^{2+} and Ar^{3+} fractions (see Pérez-Montero 2017). However, the weak $[ArIV]4740\text{\AA}$ line at the edge of our wavelength range has a weak signal-to-noise in our observations, as inferred from the skewed distribution on its abundance determination.

The total abundances are tabulated in Table 4 and Fig.5 displays the same results graphically over the CGCG007-025 $H\alpha$ map.

3.3 Photoionization model fitting

Simulating the observable parameters from a grid of conditions, for both the ionizing source and the surrounding gas, provides astronomers with a powerful tool to understand the star formation phenomena. In this work, we compare two techniques to fit models from the PopSTAR evolutionary synthesis grids by Mollá et al. (2009); Martín-Manjón et al. (2010). These models were compiled by Pérez-Montero (2014) with an initial mass function of Chabrier (2003) and a burst age of 1 Myr. The model metallicity is scaled to the solar value with the oxygen abundance. The models parameterise the variation of the N/O ratio from its dependence on the $[NII]$ line fluxes as the N/H abundance changes. The electron density is constant with 100 cm^{-3} , as well as, the cluster age of 1 Myr. The grids were generated using CLOUDY v17 by Ferland et al. (2017) with the following ranges: $7.1 \leq 12 + \log(O/H) \leq 9.0$, $-2.0 \leq \log(N/O) \leq 0$ and $-4.0 \leq \log(U) \leq -1.5$. As in the direct method treatment, we are excluding those lines suspected of saturation (see section 2).

3.3.1 HII-CHI-MISTRY sampling

The first tool to fit the photoionization model is HII-CHI-MISTRY v5.22. The complete algorithm description can be found in Pérez-Montero (2014); Pérez-Montero et al. (2019, 2021), but at its core, the sampling consists in three interpolations. The grid described in the previous subsection is treated as a 3-dimensional array. The first interpolation is across the N/O axis as a function of the $[NII]6584\text{\AA}$ fluxes. The second interpolation anchors the $12 + \log(O/H)$ abundance. Finally, the algorithm fits the ionization parameter, $\log(U)$, according to the input lines. Additionally, the algorithm includes several empirical models to constrain the sampled parameters, in those cases where not all the model input lines are available.

Table 4 includes the results from the HII-CHI-MISTRY fittings. Each row corresponds to one of the model parameters, while the first column contains the average result from all the voxels while in the subsequent columns present the distributions from the spatial signal-to-noise masks described in 2. In addition to the PopSTAR configuration, the algorithm was configured to use the interpolation feature to increase the grid resolution. Moreover, the default Monte Carlo chain length was increased from 25 to 200. Unfortunately, due to the partial overlap between MUSE wavelength range and HII-CHI-MISTRY input lines, only $[OIII]4959\text{\AA}$, $[OIII]5007\text{\AA}$, $[NII]6584\text{\AA}$, $[SII]6716\text{\AA}$ and $[SII]6731\text{\AA}$ are used as inputs. The line fluxes are corrected from the dust extinction using the voxel $c(H\beta)$ calculated in section 3.1.

3.3.2 Neural network sampling

The second approach to fit the photoionization model is using the neural networks sampler from the direct method treatment. This approach was first introduced in the chemical analysis of the three Green Peas galaxies in Fernández et al. (2021). At the time, it was argued that this scheme provided a faster treatment, while making possible the sampling of grids with a higher number of dimensions and input lines. At this point, we perform three quality checks on this methodology:

Firstly, we try to fit as many lines as possible from the complete photoionization grid of HII-CHI-MISTRY ((Pérez-Montero et al. 2021, private communication). Indeed, the number of input lines is almost the same as in the direct method treatment. Some of the lines not included are the hydrogen Paschen lines. However, since the fluxes are corrected from the dust extinction using the coefficients in section 3.1, the hydrogen transitions do not supply additional information to the fitting.

Secondly, we perform a systematic analysis on the algorithm convergence for the grid parameter space. At seven points per $12 + \log(O/H)$, $\log(N/O)$ and $\log(U)$ axis, we get the line fluxes within the MUSE wavelength range. Afterwards, these fluxes are introduced into the neural sampler to fit the model parameters. The results from these tests can be found in the 3-dimensional scatter plots in Fig. 6. Each point represents 10 fittings, one per processor-thread, consisting in 2500 steps Monte-Carlo chains. The first 500 steps are excluded from the measurement statistics, since they represent the time it takes the simulation to reach the solution coordinate. On the left hand side plot of Fig. 6, the dots color represent the Gelman-Rubin or \hat{R} statistic (see Gelman & Rubin 1992). This is the ratio of the variance of the combined 10 chains (20000 points in this case) by the averaged variance of the individual chains. In an ideal output, this ratio should be one. In the PyMC3 sampler, chains with $\hat{R} > 1.4$ are labelled with an unsuccessful convergence. Similarly, the dot colors in the second graph quantify the 3 parameters average deviation from their true values. From these diagrams it can be concluded that the algorithm has in general, a very good convergence at the true values. The exception lies on the higher metallicity end. Looking at the individual traces (check Fig. 4 in Fernández et al. 2021), some of the chains are stuck grid edge values. Moreover, we find that while there is convergence at the lower $\log(U)$ boundary, the code is not finding the true solutions. Consequently, parameter measurements from these regions in real spectra should be regarded with suspicion.

Finally, in this work we explore the impact of the input lines uncertainty on the photoionization model fitting. The tabulated data in Table 4 show the results from different configurations. As in the direct method analysis, the Bayesian likelihood is defined with a normal distribution. This is further discussed in the next section.

Unlike in the direct method analysis, the sampling uses an automatic differentiation variational inference (ADVI) to set the threads initial values. Testing the inbuilt algorithms in PyMC, this is the one with the best convergence for the parameter space.

4 DISCUSSION

The chemical analysis of CGCG007-025 shows a normal spatial distribution for most parameters. The exceptions to this pattern are the dust extinction and the electron density. The results are tabulated in Table 3 and Table 4. The same results are displayed graphically in Fig. 5 and Fig. 7. In the spectrophotometric catalogue of low metallicity compact HII galaxies of Terlevich et al.

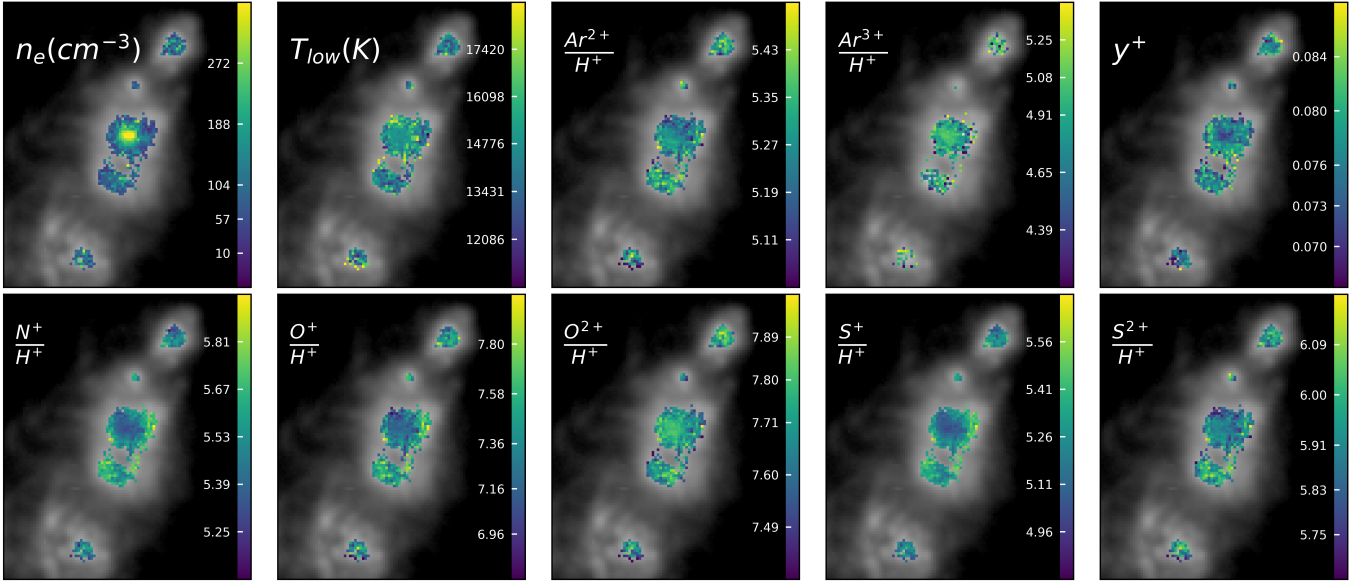


Figure 5. Voxel measurements for the n_e , T_{low} and ionic abundances (in $12 + \log(X^{i+}/H)$ scale) from the direct method. The tabulated values on the color bars correspond to the median, $P_{16th}-P_{84th}$ and $2 \times P_{16th}-P_{84th}$. The $c(H\beta)$ maps are excluded from this figure since its distributions can be better appreciated from Fig. 4. The background gray-scale voxels correspond to the MUSE $H\alpha$ band.

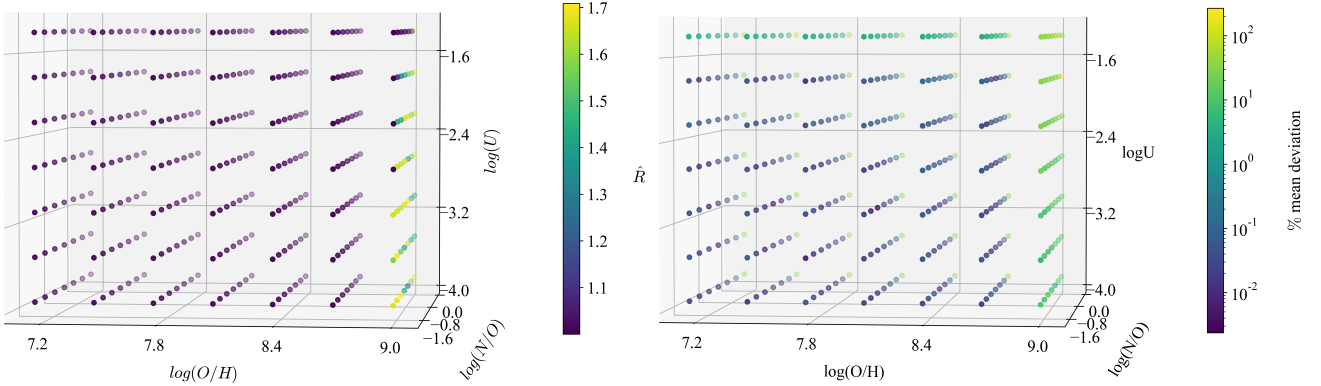


Figure 6. Scatter plots with the diagnostics for the neural photoionization fitting of the MUSE range lines from the POPSTAR grid described in section 3.3. Each point represents 10 fittings with a 2500 steps per thread. Left) The color scale represents the mean Gelman-Rubin (\hat{R}) statistic calculated from the 3 parameter output chains. Fittings with $\hat{R} > 1.4$ have failed to converge. Right) The mean discrepancy for the three parameters with their true value.

(1991), the $c(H\beta)$ distribution of the 425 galaxies peaked in the $c(H\beta) \approx 0.2 - 0.3$ range. This is the regime observed for most of the central clump (region 1) and north and south clumps (region 2). However, at the core of the central clump, where the brightest voxels are found, the extinction of the galaxy is almost three times higher ($c(H\beta) = 0.52 \pm 0.06$) than the mean value of the 73 voxels, ($c(H\beta) = 0.21 \pm 0.08$). Despite the dead and saturated-risk pixels at the $H\alpha$ line. This steep extinction gradient is observed in the 4 most intense Paschen lines (HI_{P12} 8750Å, HI_{P11} 8863Å, HI_{P10} 9015Å and HI_{P9} 9229Å). This can be appreciated in Fig. 4. Additionally, the same behaviour is observed in the electron density measurements. The average density of CGCG007-025, $n_e = 104 \pm 84 \text{ cm}^{-3}$, is a standard value for low metallicity star forming galaxies (see Hägle et al. 2008). In contrast, the central knot has densities thrice times higher, $n_e = 378 \pm 63 \text{ cm}^{-3}$.

Published studies on CGCG007-025 have found similar parameter values. While van Zee (2000) presented a photometric dwarf sam-

ple with both CGCG007-025 and its neighbour UGC5202, van Zee & Haynes (2005) focused on the gas compositions of dwarfs with intense star formation. The latter work included three slits on the central cluster of CGCG007-025. These extinctions were $c(H\beta)_W = 0.22 \pm 0.05$, $c(H\beta)_N = 0.31 \pm 0.04$ and $c(H\beta)_S = 0.12 \pm 0.05$. The authors manuscript did not tabulate the electron densities but from the reported [SII] ratios we can measure $n_{e,W} = 119 \pm 94$, $n_{e,N} = 189 \pm 124$ and $n_{e,S} = 162 \pm 118 \text{ cm}^{-3}$. Senchyna et al. (2017) studied the ultraviolet emission of CGCG007-025 (labelled as SBID 2) using the HST/COS observations. Their work also includes a chemical analysis with SDSS and MMT spectra. The authors presented an extinction coefficient of $c(H\beta) = 0.21 \pm 0.07$ and an electron density of $n_e = 186^{+33}_{-32} \text{ cm}^{-3}$. Izotov and collaborators have included CGCG007-025 in several of their papers focused on the primordial helium abundance determination. Finally, CGCG007-025 gas composition has been analysed by the CLASSY team. Arellano-Córdova et al. (2022b) explores the aperture effects

on this sample by comparing twelve APO/SDSS long-slit spectra, seven LBT/MODS long-slit spectra and three LBT/MUSE IFU cubes and six Keck/ESI echelle spectra. The authors find that the density and extinction remain roughly uniform across the three data sets. Their IFU sub-sample does not include CGCG007-025. However, they warned that in their 3 IFUs, the extinction magnitude decreases up to 53% from the center of the galaxy. Moreover, similar behaviour was observed while investigating the aperture extraction on the IFU $[SII]6716\text{\AA}, 6731\text{\AA}$ doublet band. Higher values were found at the center of the galaxies. The extinction reported for CGCG007-025 was $c(H\beta) \approx 0.24$ from the three longslit data sets. The reported mean density from the $[SII]$ lines was $\approx 120\text{ cm}^{-3}$. Additionally, the authors report the density from the $[OII]3727\text{\AA}, 3729\text{\AA}$ doublet from extinction measured with the LBT/MODS spectrum. This value was considerably higher with $n_e[OII] = 480 \pm 170\text{ cm}^{-3}$. This value was above the 100 cm^{-3} mean discrepancy found between the $[OII]$ and $[SII]$ densities (the latter always lower) for the CLASSY sample. In conclusion, the literature results agree with the spatial distribution measured in this paper.

The cause behind the spatial variation on these parameters may be found in the evolutionary state of the central clump in CGCG007-025. The value of $c(H\beta)$ (as well as the color excess, E_{B-V}) depends on the grain properties (composition and size) and the column density in the line of sight (see chapter 7 of [Osterbrock 1974](#)). Assuming the same dust type, the higher extinction can be explained by a denser medium. In our Galaxy, the dust extinction per unit column density of hydrogen, $A_V/N(H)$, displays similar values from stellar samples as confirmed by [Bohlin et al. \(1978\)](#) and [Rachford et al. \(2008\)](#). As a loose proxy, we can use the $c(H\beta)/n_{SII}$ resulting in 0.0014, 0.0015 and 0.002 for regions 0, 1 and 2. The spatial distribution of this ratio is rather uniform across the galaxy central clump. More-alike the behaviour of the other chemical measurements. CGCG007-025 was one of the test cases for the spectral synthesis library FADO by [Gomes & Papaderos \(2017\)](#). The fiber from the SDSS spectrum was centered at the central clump of CGCG007-025 and the light-weighted age resulted in a value of $\log(Age)_L = 6.34\text{ yr}$. Our stellar synthesis on the complete MUSE region agrees with this result, while confirming an older stellar population in the outer regions. Consequently, the density inhomogeneities can be explained by a very young cluster at the core. These measurements, however, will have their dedicated analysis in future work by (Sánchez-Janssen et al, in preparation).

The previous bibliography includes the measurements of the electron temperature, mainly, from the auroral $[OIII]4363\text{\AA}$ line. In [van Zee & Haynes \(2005\)](#) three WN, W and S slits, the measurements were: $T[OIII] = 14770^{530}_{500}\text{ K}$, $16010^{340}_{330}\text{ K}$, $13920^{500}_{430}\text{ K}$. These results lead to an oxygen abundance of 7.83 ± 0.03 , 7.78 ± 0.03 and 7.85 ± 0.03 respectively. In contrast, the analysis of [Senchyna et al. \(2017\)](#), combining the SDSS and the MMT fluxes (for the $[OII]3727, 3729\text{\AA}$ doublet) resulted in $T[OIII] = 15800 \pm 500\text{ K}$ and $12 + \log(O/H) = 7.81 \pm 0.07$. The two long-slit spectra in [Izotov & Thuan \(2004\)](#) include both the O^{2+} and S^{2+} temperatures, where: $T[OIII]_1 = 16470 \pm 170\text{ K}$, $T[OIII]_2 = 16560 \pm 260\text{ K}$ and $T[SIII]_1 = 15370 \pm 140\text{ K}$, $T[SIII]_2 = 15440 \pm 260\text{ K}$. The reported oxygen and sulphur abundances were $12 + \log(O/H) = 7.775 \pm 0.010$, 7.738 ± 0.013 and $12 + \log(S/H) = 5.92 \pm 0.01$, 5.87 ± 0.03 . Finally, the mean CLASSY measurements from [Arellano-Córdova et al. \(2022b\)](#) ground telescopes compilation have a mean temperature of $T[SIII] \approx 14500\text{ K}$ and $T[OIII] \approx 15500\text{ K}$. The mean oxygen abundance was $12 + \log(O/H) \approx 7.79$. The authors concluded that the aperture effects on the metallicity measurements is $< 0.1\text{ dex}$. Our results agree with this estimation.

The variability in the chemical content of CGCG007-025 found

in the literature above (and others not discussed, see [Knizhev et al. 2004](#); [Guseva et al. 2007](#); [Shirazi & Brinchmann 2012](#); [Chevallard et al. 2018](#); [Kurichin et al. 2021](#)) can be explained by the spatial distribution observed in this work. In the case of the oxygen abundance, distribution measured are 7.88 ± 0.03 , 7.87 ± 0.09 are 7.88 ± 0.12 for the voxels in regions 0, 1 and 2 respectively. Within the core of the galaxy (the brightest knot with 11 voxels $\approx 48\text{ pc}$ radius), the ionic abundance the variation is below 0.05 dex. This sigma can be explained by the uncertainty on the flux measurement. Mainly, from the $[SIII]6312\text{\AA}$ temperature diagnostic line. However, once we start to consider the remaining 91 and 382 voxels (with radii $\approx 140\text{ pc}$ and 382 pc respectively), the dispersion on the parameters can no longer be explained by the flux measurement uncertainty. From the data in Table 3, the 484 voxels ratio between their ionic abundances distributions sigma and their uncertainty distribution sigma is $\sigma_{\text{measurement}}/\sigma_{\text{uncertainty}} \approx 2.1$. Looking at the spatial maps in Fig.5, however, there isn't a distinctive gradient on these parameters (except for $c(H\beta)$ and n_e as discussed previously). In well observed objects, such as our Galaxy or Messier33, a chemically homogeneous gas has been reported, (see [Esteban et al. 2022](#); [Rogers et al. 2022](#), respectively). This is because the galactic structure provides well-mixed enriched from inside out enrichment. In an compact system such as CGCG007-025, however, this points towards a very sudden starburst, fueled by fresh metal-poor gas.

This chemical distribution places CGCG007-025 within the Extreme Emission Line Galaxies (EELGs) family. These objects are characterised by their dominant nebular component (which hides the underlying galaxy stellar continuum), compact sizes and low metallicities (see [Smit et al. 2014](#); [Amorín et al. 2014](#); [Roberts-Borsani et al. 2016](#); [Stark et al. 2017](#); [Calabrò et al. 2017](#); [Tang et al. 2019](#)). These properties are expected to be more common in the early universe, (see [Atek et al. 2014](#); [Amorín et al. 2017](#); [Maseda et al. 2018](#); [Endsley et al. 2021](#)). Nonetheless, in the nearby universe, $z \approx 0.14 - 0.36$, Green Pea galaxies (GPs), are being targeted as analogues at the lower redshift (see [Cardamone et al. 2009](#)). These objects have small sizes, with few or below 1 kpc effective radius (see [Amorín et al. 2012](#); [Yang et al. 2017](#)) and stellar masses below $\log(M_*) < 10M_\odot$. This is the case of CGCG007-025 whose reported neutral hydrogen mass is $\log(M(HI)) = 8.62M_\odot$ (see [van Zee 2001](#)), dynamical mass $\log(M_{dyn}) = 9.36M_\odot$ (see [van Zee & Haynes 2005](#)) and stellar mass $\log(M_*) = 8.17M_\odot$ (see [Gavilán et al. 2013](#)). The oxygen abundance in these objects is around 20% the solar value, $7.4 < 12 + \log(O/H) < 8.4$ (see [Amorín et al. 2010](#); [Pérez-Montero et al. 2021](#); [Fernández et al. 2021](#)). All these properties are within the gas emission characteristics measured here for CGCG007-025.

4.1 Radiation field and photoionization model fitting implications

In addition to the gas properties, the emission fluxes can provide constraints on the ionization source of a star forming region. This methodology is known as photoionization model fitting. [Stasinska \(2007\)](#) describes it as the "royal" approach to analyse emission line spectra. Moreover, this review illustrates its common challenges: "How to explore the parameter space? How to deal with error bars? How to test the model validity?". While the latter issue is within the astrophysicist responsibilities, the former two are heavily affected by the researcher mathematical/computational resources. We take advantage of this work on CGCG007-025 to propose a to anchor the parameter space exploration and the error bar definition.

In section 3.3.2, we presented the sampling algorithm alongside

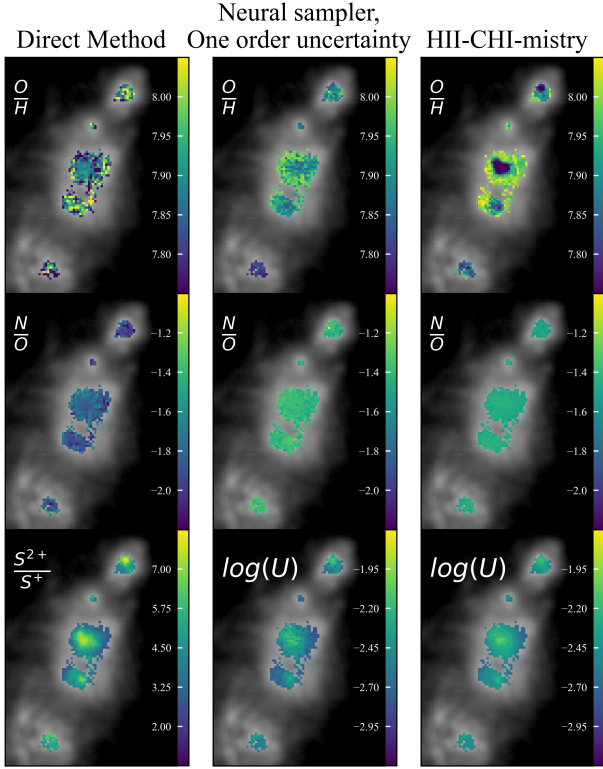


Figure 7. Comparison between the photoionization model fitting techniques and the direct method. Instead of $\log(U)$, we use S^{2+}/S^{+} as a proxy in the direct method. In the oxygen distribution map, the color bar tabulated values are fixed. In the remaining maps, the color bars display the median, P_{16th} - P_{84th} and $2 \times P_{16th} - P_{84th}$. The background gray-scale voxels correspond to the MUSE cube $H\alpha$ band.

the convergence tests for the observed transitions in the MUSE wavelength range. For these inputs, we tested the convergence stability for the models $\log(U)$, $12 + \log(O/H)$ and $\log(N/O)$ parameter space. At this point, knowing from the direct method the CGCG007-025 $12 + \log(O/H) = 7.88 \pm 0.10$ and $\log(N/O) = -1.84 \pm 0.12$ distributions, we can expect the sampler to provide stable and accurate solutions for this galaxy (within the theoretical model assumptions).

The next step consists in measuring the impact of the error bars on the photoionization model fitting. In Bayesian inference, introducing the measurement error is non-trivial. In this paradigm, the variation on a datum value has nothing to do with observational constraints or instrument limitations. Instead, this dispersion around a mean value is an intrinsic physical property. A major consequence of this interpretation is that the parameters can be modelled by a probabilistic distribution. In Fernández et al. (2019), the solution proposed was defining a Bayesian likelihood per line, with a normal distribution whose sigma is the line flux uncertainty. Consequently, lines with a larger error have wider likelihoods, which have similar probabilities for a wider range of the parameter values. This is still the approach in the direct method fitting. Moreover, this is the configuration in second row of Table 4 labelled as "observed line fluxes and uncertainty" for the photoionization model fitting. The next row contains the results for the "HII-CHI-MISTRY inputs". In this case, we use the observed fluxes and uncertainty but we only introduced the same lines as in HII-CHI-MISTRY. In the next test case in Table 4 "Uniform maximum

observed uncertainty" we overestimate the uncertainty of all the lines to the maximum uncertainty from the input emission spectra. Finally, in the "One order uncertainty range" we overestimate the minimum flux uncertainty one order below the maximum one. For example, if the $[NII]6784\text{\AA}$ line has 20% flux uncertainty, the flux uncertainty of the $[OIII]5007\text{\AA}$ flux is overestimated to 2%.

The results from the photoionization model fitting and the comparison between the direct method lead to the following insights:

- The measurements from HII-CHI-MISTRY confirm a hard ionization in CGCG007-025 with a mean ionization parameter of $\log(U) = -2.44^{+0.17}_{-0.14}$ for all the voxels. This value decreases from $-2.14^{+0.06}_{-0.04}$ at the central knot where the most intense cluster is found to a mean value $-2.47^{+0.13}_{-0.12}$ including voxels in the north, south and outskirts of the central clump. In Fig. 5, we can see that there is a small west offset between the central knot and the highest $\log(U)$ values. The neural sampler finds values within 0.05 dex with the same spatial behaviour and with slightly higher uncertainty in the measurement. Senchyna et al. (2017) provided a measurement for this parameter of $\log(U) = -4.00 \pm 0.25$ from the ultraviolet fluxes of CGCG007-025. However, this value was calculated from the photoionization models of Gutkin et al. (2016) where $\log(U) = -4.00$ is the lowest value from the grid. This suggest a typo or issues during the model fitting. Even though there isn't an equivalent for $\log(U)$ in the direct method, we have included the S^{2+}/S^{+} map on Fig. 5. We can observe the same spatial behaviour on this proxy.

- The mean nitrogen excess reported by HII-CHI-MISTRY is $\log(N/O) = -1.47^{+0.03}_{-0.04}$. This value is significantly larger than the direct method measurement at $\log(N/O) = -1.84^{+0.12}_{-0.12}$. The results from the neural sampler are similar with slightly lower mean values. Moreover, for all the photoionization model fitting approaches the uncertainty varies very little across the galaxy. This discrepancy can be explained by the degeneracy of the models with the nitrogen excess. This can be appreciated in the left plot of Fig. 8. Looking at the $[NII]6584\text{\AA}$ grid as a function of $\log(N/O)$, for values $\log(N/O) < 1.25$ the increase in the relative $[NII]$ photon flux is below 3% in $7.60 < 12 + \log(O/H) < 8.00$ range. At this regime the oxygen abundance (which parameterises the metallicity in this model) has a greater impact on the model nitrogen transition flux. Consequently, for a galaxy such as CGCG007-025 with very little $\log(N/O)$ excess, anchoring the parameter is challenging. The long-slit observations by Izotov & Thuan (2004) reported $\log(N/O)_1 = -1.622 \pm 0.014$ and $\log(N/O)_2 = -1.622 \pm 0.014$. In contrast, from the three slits of van Zee & Haynes (2005) the measurements were $\log(N/O)_W = -1.55 \pm 0.07$, $\log(N/O)_N = -1.47 \pm 0.06$, $\log(N/O)_S = -1.47 \pm 0.06$.

- The oxygen abundance measured by HII-CHI-MISTRY shows a large spatial gradient compared with the direct method. At the central knot, the oxygen content is 0.15 dex lower, with a 0.01 dex sigma. In contrast, the outer voxels mean value is 0.1 dex higher, though with a skewed uncertainty at $12 + \log(O/H) = 7.98^{+0.04}_{-0.11}$ for lower values. This issue can be appreciated on the right hand side plot in Fig. 8. The plot shows a few emission line fluxes evolution with $\log(U)$ at $12 + \log(O/H) = 7.80$. In the $-2.5 < \log(U) < -2.0$ range, $[OIII]$ and $[OII]$ fluxes have a well define behaviour unlike other input fluxes. However, without the $[OII]$ fluxes in the fitting there is a great degeneracy to anchor the O^{+} content. Consequently, at the high ionization voxels, where the O^{+} fraction is expected to be smaller the oxygen abundance is underestimated, while overestimated at lower $\log(U)$ values. This can be appreciated in Fig. 7 where the HII-CHI-MISTRY metallicity decreases in regions as the $\log(U)$ increases.

- In the neural sampler, those configurations with

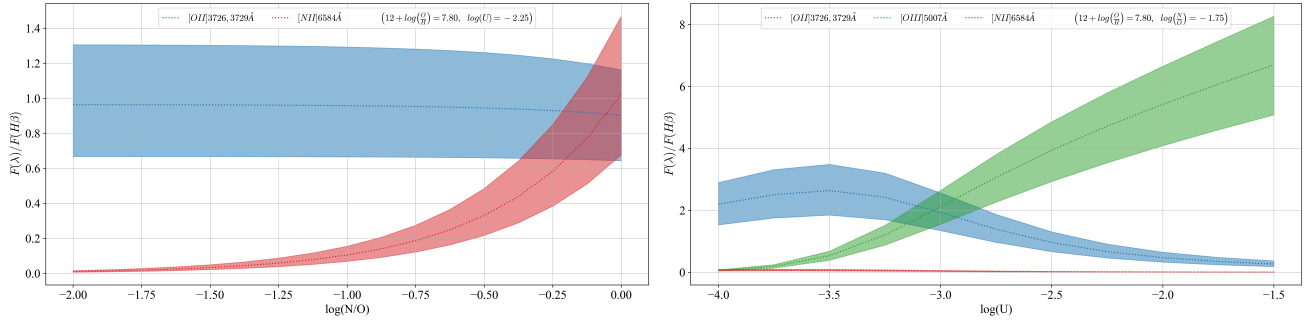


Figure 8. Theoretical fluxes from the photoionization model grids versus the model parameters. a) Evolution of $[OII]3727, 3729\text{\AA}$ and $[NII]6584\text{\AA}$ as a function of the $\log(N/O)$ excess. b) Evolution of $[OII]3727, 3729\text{\AA}$, $[OIII]5007\text{\AA}$ and $[NII]6584\text{\AA}$ with the ionization parameter. In both plots the dashed lines represent the fluxes for $12 + \log(O/H) = 7.80$ while the dashed areas cover the $\Delta(O/H) = \pm 0.20$ interval in the same scale.

$[OII]7319, 7330\text{\AA}$ had a better match with the oxygen abundance from the direct method. It should be noted, however, that there isn't an abundance underestimation at the central core unlike in the case of HII-CHI-MISTY. This can be explained by the fact that in this techniques all lines are contributing to all the parameters fitting. Consequently, the $[SII]$ and $[NII]$ fluxes are anchoring the metallicity fraction from the low ionization potential species.

- In region 2 voxels, where lower signal-to-noise, and hence higher flux uncertainty is observed, all photoionization models displayed a lower parameter uncertainty than the direct method. In the neural sampler, it is possible to compare the fit fluxes against the observational ones as a quality check. It was appreciated that once there is an important uncertainty discrepancy, the algorithm will "neglect" the weaker lines. This means that while $[OIII]$ fluxes have a better match with the models, the weaker lines show discrepancies above 100%. Using the maximum line uncertainty for all the lines provided a more uniform mismatch between the line fluxes and the models. However, as we can see in Table 4, this increased the discrepancy with the direct method measurement. As a compromise, the last configuration overestimates the minimum flux uncertainty one order below the line with the largest flux error. This provides the best fidelity between the flux across the lines and the measurements with from the direct method. Still, this method has a better precision than the direct method.

The previous observations ratify the position of CGCG007-025 as an EELG. Recently, [Díaz & Zamora \(2022\)](#) analysed the composition of high quality observations of diffuse HII regions and HII galaxies. The first group includes star forming bursts in irregular, spiral galaxies, as well as, our own Galaxy. The second group labels blue compact dwarfs, whose luminosity is dominated by the gas emission. The selection criteria is $E_{q\omega}(H\beta) > 50\text{\AA}$, which imposes a maximum stellar cluster age around 7 Myr (see [Terlevich et al. 2004](#)). The chemical properties of CGCG007-025 lie at the outskirts of the lowest metallicity diffuse HII regions or the typical values of HII galaxies. The oxygen and sulfur median abundance in this family sample were $12 + \log(O/H) = 7.85$ and $12 + \log(S/H) = 6.27$ with ranges of $7.0 - 8.5$ and $5.7 - 7.25$ respectively. The remaining properties in Table 3 are also well represented by the HII galaxy family. The $\log(S/O) = -1.73 \pm 0.074$ distribution from all the voxels matches the $-1.9 \lesssim \log(S/O) \lesssim -1.3$ regime observed by [Díaz et al. \(1991\)](#); [Dors et al. \(2016\)](#); [Díaz & Zamora \(2022\)](#) with ratios below solar, $(\log(S/O))_{\odot} = 1.6$. Finally, the radiation softness

parameter introduced by [Vilchez & Pagel \(1988\)](#) can be used to map the radiation hardness. This is defined as:

$$\eta = \frac{O^+/O^{++}}{S^+/S^{++}} \quad (4)$$

In CGCG007-025, the median value for eq.4 numerator is ≈ 2.2 while its denominator is ≈ 4.5 . We find that for both elements, the twice-ionized atoms dominate the abundance. However, we observed that $S^+/S^{++} \approx 2 \times O^+/O^{++}$. This is a common value for low metallicity, high star formation HII galaxies (see [Díaz & Zamora 2022](#)). The mean $\log(\eta) \approx -0.3$ value is common in HII galaxies (see [Hägele et al. 2006](#); [Kumari et al. 2021](#)).

5 CONCLUSIONS

At $z = 0.00469$, the CGCG007-025 - UGC5205 galaxy pair represents a unique system for the study of star formation. While the former is a gas-rich galaxy undergoing a star forming burst, the latter is almost gas depleted. This manuscript is the first study on the pair by the authors, with a focus on the chemical content of CGCG007-025 using an archive MUSE IFU observation. The authors took this opportunity to test novel algorithms for the treatment of large data sets while maintaining a tailored analysis on the emission features. The main takeaways from this work are:

- Over 60000 lines were measured in 7774 voxels. These voxels were organized in a set of masks according to the signal-to-noise of $H\alpha$ and our temperature diagnostic line, $[SII]6312\text{\AA}$. This was done with LiMe, a python library developed by the authors for the detection, measurement and profile fitting of lines in astronomical spectra. The library is fully documented and this is the beta release for the community.

- The MUSE cube was analysed with the stellar synthesis code FADO, which takes into consideration the nebular continua. The absorptions on the HI and HeI transitions were measured to correct the emission features for the extinction and helium abundance calculation. A future manuscript will focus on the stellar populations of the galaxy pair.

- The extinction was measured across the galaxy by comparing the ratio between the observed hydrogen fluxes and their theoretical emissivities. At the center of the galaxy, where the brightest star formation clump is found, there is a photon drop in $H\alpha$ and $[OIII]5007\text{\AA}$. This is likely due to a loss in CCD linearity at the high flux rate from these transitions. However, the extinction could be measured accurately in this region thanks to the Paschen transitions

which could be accurately measured at this region. The logarithmic extinction coefficient decreases sharply from $c(H\beta) = 0.50 \pm 0.06$ at the core to the mean value of the galaxy at $c(H\beta) = 0.11 \pm 0.11$. This higher extinction can be explained by the higher density of a very young stellar cluster of $r \approx 48 pc$.

- The direct method was applied on 484 voxels with good $[SII]6312\text{\AA}$ detection. The methodology consists in a previously published neural network sampler, which fits the entire parameter space simultaneously. The spatial analysis shows normal distributed content for the analysed oxygen, nitrogen, sulfur, helium and argon ionic species. In the case of oxygen, this distribution is $12 + \log(O/H) = 7.88 \pm 0.11$. Around half this dispersion can be explained by the uncertainty flux measurement. Except for n_e and $c(H\beta)$, there is a weak gradient on these abundances.

- Since HII-CHI-MISTRY inbuilt library does not include the $[OII]7319, 7330\text{\AA}$ lines, the algorithm had issues to anchor the oxygen abundance. The neural sampler managed to reproduce the expected results once these lines were introduced. Both approaches, however, had issues fitting the $\log(N/O)$ excess due to the grid degeneracy at this galaxy low $\log(N/O) = -1.84 \pm 0.12$ value. Finally, the models predict a hard ionization field with $\log(U) = -2.44^{+0.17}_{-0.14}$.

- Taking advantage of the neural networks speed and efficiency to explore complex parameter spaces, we developed a workflow to test the convergence on the model grid of HII-CHI-MISTRY. The results were satisfactory and the measurements on CGCG007-025 managed to overcome the issues with the limited inputs of HII-CHI-MISTRY. Finally, the authors run several Bayesian likelihood configurations to establish the impact of the flux uncertainty on the parameter measurements. The authors recommend to put a limit on the minimum the uncertainty of the fluxes. This way, both auroral and nebular contribute to the sampling and the results are equivalent to those from the direct method. This sigma limit is one order below the uncertainty of the line with the largest uncertainty.

All these properties place CGCG007-025 in the extreme emission line galaxy family. This makes the galaxy ecosystem an ideal candidate to understand young star formation episodes at low metallicity, which are common at high redshift. Future work will include new observations and methodologies, to explain the phenomena observed.

ACKNOWLEDGEMENTS

The authors also wish to thank an anonymous referee, whose comments helped to improve the clarity of the paper. V.F. acknowledges financial support provided by FONDECYT grant 3200473. R.A. acknowledges support from ANID Fondecyt Regular 1202007. P.P. thanks Fundação para a Ciência e a Tecnologia (FCT) for managing research funds graciously provided to Portugal by the EU. This work was supported through FCT grants UID/FIS/04434/2019, UIDB/04434/2020, UIDP/04434/2020 and the project "Identifying the Earliest Supermassive Black Holes with ALMA (IdEaS with ALMA)" (PTDC/FIS-AST/29245/2017). M.G.V.E acknowledges the support of the UK Science and Technology Facilities Council

DATA AVAILABILITY

The inclusion of a Data Availability Statement is a requirement for articles published in MNRAS. Data Availability Statements provide a standardised format for readers to understand the availability of data underlying the research results described in the article. The statement may refer to original data generated in the course of the study or to

third-party data analysed in the article. The statement should describe and provide means of access, where possible, by linking to the data or providing the required accession numbers for the relevant databases or DOIs.

REFERENCES

- Ahumada R., et al., 2020, *The Astrophysical Journal Supplement Series*, 249, 3
- Amorín R., Pérez-Montero E., Vílchez J. M., 2010, *The Astrophysical Journal*, 715, L128
- Amorín R., Pérez-Montero E., Vílchez J. M., Papaderos P., 2012, *The Astrophysical Journal*, 749, 185
- Amorín R., et al., 2014, *The Astrophysical Journal*, 788, L4
- Amorín R., et al., 2017, *Nature Astronomy*, 1, 0052
- Arellano-Córdova K. Z., et al., 2022a, A First Look at the Abundance Pattern – O/H, C/O, Ne/O, and Fe/O – in $z > 7$ Galaxies with JWST/NIRSpec, doi:10.48550/arXiv.2208.02562, <http://arxiv.org/abs/2208.02562>
- Arellano-Córdova K. Z., et al., 2022b, *The Astrophysical Journal*, 935, 74
- Atek H., et al., 2014, *The Astrophysical Journal*, 789, 96
- Bacon R., et al., 2010, in Ground-based and Airborne Instrumentation for Astronomy III. SPIE, pp 131–139, doi:10.1117/12.856027, <https://www.spiedigitallibrary.org/conference-proceedings-of-spie/7735/773508/The-MUSE-second-generation-VLT-instrument/10.1117/12.856027.full>
- Bacon R., Piqueras L., Conseil S., Richard J., Shepherd M., 2016, *Astrophysics Source Code Library*, p. ascl:1611.003
- Berg D. A., et al., 2022, *The Astrophysical Journal Supplement Series*, 261, 31
- Birkmann S. M., et al., 2022, Technical report, The In-Flight Noise Performance of the JWST/NIRSpec Detector System, <https://ui.adsabs.harvard.edu/abs/2022arXiv220812686B>, <https://ui.adsabs.harvard.edu/abs/2022arXiv220812686B>
- Bohlin R. C., Savage B. D., Drake J. F., 1978, *The Astrophysical Journal*, 224, 132
- Brinchmann J., 2022, Technical report, High-z galaxies with JWST and local analogues – it is not only star formation, <https://ui.adsabs.harvard.edu/abs/2022arXiv220807467B>, <https://ui.adsabs.harvard.edu/abs/2022arXiv220807467B>
- Calabrò A., et al., 2017, *Astronomy & Astrophysics*, 601, A95
- Cardamone C., et al., 2009, *Monthly Notices of the Royal Astronomical Society*, 399, 1191
- Carnall A. C., et al., 2022, A first look at the SMACS0723 JWST ERO: spectroscopic redshifts, stellar masses and star-formation histories, doi:10.48550/arXiv.2207.08778, <http://arxiv.org/abs/2207.08778>
- Chabrier G., 2003, *Publications of the Astronomical Society of the Pacific*, 115, 763
- Chevallard J., et al., 2018, *Monthly Notices of the Royal Astronomical Society*, 479, 3264
- Curti M., et al., 2022, The chemical enrichment in the early Universe as probed by JWST via direct metallicity measurements at $z \sim 8$, doi:10.48550/arXiv.2207.12375, <http://arxiv.org/abs/2207.12375>
- Díaz A. I., Zamora S., 2022, *Monthly Notices of the Royal Astronomical Society*, 511, 4377
- Dors O. L., Pérez-Montero E., Hägele G. F., Cardaci M. V., Krabbe A. C., 2016, *Monthly Notices of the Royal Astronomical Society*, 456, 4407
- Dufton P. L., Hibbert A., Kingston A. E., Doschek G. A., 1982, *The Astrophysical Journal*, 257, 338
- Díaz A. I., Terlevich E., Vílchez J. M., Pagel B. E. J., Edmunds M. G., 1991, *Monthly Notices of the Royal Astronomical Society*, 253, 245
- Endsley R., Stark D. P., Chevallard J., Charlot S., 2021, *Monthly Notices of the Royal Astronomical Society*, 500, 5229
- Esteban C., Méndez-Delgado J. E., García-Rojas J., Arellano-Córdova K. Z., 2022, *The Astrophysical Journal*, 931, 92

- Ferland G. J., et al., 2017, arXiv:1705.10877 [astro-ph]
- Fernandes R. C., Mateus A., Sodré L., Stasińska G., Gomes J. M., 2005, *Monthly Notices of the Royal Astronomical Society*, 358, 363
- Fernández V., 2018, PhD thesis, INAOE, Tonantzintla, Puebla, Mexico
- Fernández V., Terlevich E., Díaz A. I., Terlevich R., Rosales-Ortega F. F., 2018, *Monthly Notices of the Royal Astronomical Society*, 478, 5301
- Fernández V., Terlevich E., Díaz A. I., Terlevich R., 2019, *Monthly Notices of the Royal Astronomical Society*, 487, 3221
- Fernández V., Amorín R., Pérez-Montero E., Papaderos P., Kehrig C., Vílchez J. M., 2021, *Monthly Notices of the Royal Astronomical Society*, p. stab3150
- Foreman-Mackey D., et al., 2021, *The Journal of Open Source Software*, 6, 3285
- Galavís M. E., Mendoza C., Zeppen C. J., 1995, *Astronomy and Astrophysics Supplement Series*, 111, 347
- Galavís M. E., Mendoza C., Zeppen C. J., 1997, *Astronomy and Astrophysics Supplement Series*, 123, 159
- Gardner J. P., et al., 2006, *Space Science Reviews*, 123, 485
- Garnett D. R., 1990, *The Astrophysical Journal*, 363, 142
- Garnett D. R., 1992, *The Astronomical Journal*, 103, 1330
- Gavilán M., Ascasibar Y., Mollá M., Ángeles I. Díaz 2013, *Monthly Notices of the Royal Astronomical Society*, 434, 2491
- Gelman A., Rubin D. B., 1992, *Statistical Science*, 7, 457
- Gomes J. M., Papaderos P., 2017, *Astronomy & Astrophysics*, 603, A63
- Gomes J. M., et al., 2016, *Astronomy & Astrophysics*, 588, A68
- Gordon K. D., Clayton G. C., Misselt K. A., Landolt A. U., Wolff M. J., 2003, *The Astrophysical Journal*, 594, 279
- Guseva N. G., Izotov Y. I., Papaderos P., Fricke K. J., 2007, *Astronomy & Astrophysics*, 464, 885
- Gustavo B. A., 2001, in Vílchez J. M., Stasińska G., Pérez E., eds., *The Evolution of Galaxies: I-Observational Clues*. Springer Netherlands, Dordrecht, pp 221–230, doi:10.1007/978-94-017-3313-7_52
- Gutkin J., Charlot S., Bruzual G., 2016, *Monthly Notices of the Royal Astronomical Society*, 462, 1757
- Hudson C. E., Ramsbottom C. A., Scott M. P., 2012, *The Astrophysical Journal*, 750, 65
- Hägele G. F., Pérez-Montero E., Díaz A. I., Terlevich E., Terlevich R., 2006, *Monthly Notices of the Royal Astronomical Society*, 372, 293
- Hägele G. F., Díaz A. I., Terlevich E., Terlevich R., Pérez-Montero E., Cardaci M. V., 2008, *Monthly Notices of the Royal Astronomical Society*, 383, 209
- Izotov Y. I., Thuan T. X., 2004, *The Astrophysical Journal*, 602, 200
- Izotov Y. I., Guseva N. G., Fricke K. J., Henkel C., 2014, *Astronomy & Astrophysics*, 561, A33
- Johnson C. T., Kingston A. E., Dufton P. L., 1986, *Monthly Notices of the Royal Astronomical Society*, 220, 155
- Kaufman V., Sugar J., 1986, *Journal of Physical and Chemical Reference Data*, 15, 321
- Kniazev A. Y., Pustilnik S. A., Grebel E. K., Lee H., Pramskij A. G., 2004, *Astrophys.J.Suppl.*, 153, 429
- Kumari N., Amorín R., Pérez-Montero E., Vílchez J., Maiolino R., 2021, *Monthly Notices of the Royal Astronomical Society*, 508, 1084
- Kurichin O. A., Kislitsyn P. A., Klimenko V. V., Balashev S. A., Ivanchik A. V., 2021, *Monthly Notices of the Royal Astronomical Society*, 502, 3045
- Luridiana V., Morisset C., Shaw R. A., 2015, *Astronomy & Astrophysics*, 573, A42
- Martín-Manjón M. L., García-Vargas M. L., Mollá M., Díaz A. I., 2010, *Monthly Notices of the Royal Astronomical Society*, 403, 2012
- Maseda M. V., et al., 2018, *The Astrophysical Journal*, 865, L1
- Mendoza C., Zeppen C. J., 1982, *Monthly Notices of the Royal Astronomical Society*, 198, 127
- Mollá M., García-Vargas M. L., Bressan A., 2009, *Monthly Notices of the Royal Astronomical Society*, 398, 451
- Nair P. H., 2016, LineID Plot, doi:10.5281/zenodo.1069584, <https://zenodo.org/record/1069584>
- Newville M., Stensitzki T., Allen D. B., Ingargiola A., 2014, LMFIT: Non-Linear Least-Square Minimization and Curve-Fitting for Python, doi:10.5281/zenodo.11813, <https://zenodo.org/record/11813>
- Oey M. S., Shields J. C., 2000, *The Astrophysical Journal*, 539, 687
- Osterbrock D. E., 1974, *Astrophysics of Gaseous Nebulae*. University Science Books, <http://adsabs.harvard.edu/abs/1974agn...book.....O>
- Pagel B. E. J., Edmunds M. G., Fosbury R. A. E., Webster B. L., 1978, *Monthly Notices of the Royal Astronomical Society*, 184, 569
- Pagel B. E. J., Simonson E. A., Terlevich R. J., Edmunds M. G., 1992, *Monthly Notices of the Royal Astronomical Society*, 255, 325
- Papaderos P., et al., 2013, *Astronomy & Astrophysics*, 555, L1
- Peimbert A., Peimbert M., Luridiana V., 2016, *Revista Mexicana de Astronomía y Astrofísica*, 52, 419
- Podobedova L. I., Kelleher D. E., Wiese W. L., 2009, *Journal of Physical and Chemical Reference Data*, 38, 171
- Porter R. L., Ferland G. J., Storey P. J., Detisch M. J., 2012, *Monthly Notices of the Royal Astronomical Society: Letters*, 425, L28
- Pradhan A. K., Montenegro M., Nahar S. N., Eissner W., 2006, *Monthly Notices of the Royal Astronomical Society: Letters*, 366, L6
- Proprius R. D., Conselice C. J., Liske J., Driver S. P., Patton D. R., Graham A. W., Allen P. D., 2007, *The Astrophysical Journal*, 666, 212
- Pérez-Montero E., 2014, *Monthly Notices of the Royal Astronomical Society*, 441, 2663
- Pérez-Montero E., 2017, *Publications of the Astronomical Society of the Pacific*, 129, 043001
- Pérez-Montero E., Dors Jr O. L., Vílchez J. M., García-Benito R., Cardaci M. V., Hägele G. F., 2019, *Monthly Notices of the Royal Astronomical Society*, 489, 2652
- Pérez-Montero E., Amorín R., Sánchez Almeida J., Vílchez J. M., García-Benito R., Kehrig C., 2021, *Monthly Notices of the Royal Astronomical Society*, 504, 1237
- Rachford B. L., et al., 2008, *The Astrophysical Journal Supplement Series*, 180, 125
- Ramsbottom C. A., Bell K. L., 1997, *Atomic Data and Nuclear Data Tables*, 66, 65
- Roberts-Borsani G. W., et al., 2016, *The Astrophysical Journal*, 823, 143
- Rogers N. S. J., Skillman E. D., Pogge R. W., Berg D. A., Croxall K. V., Bartlett J., Arellano-Córdova K. Z., Moustakas J., 2022, *The Astrophysical Journal*, 939, 44
- Salvatier J., Wiecki T. V., Fonnesbeck C., 2016, *PeerJ Computer Science*, 2, e55
- Schaerer D., Izotov Y. I., Verhamme A., Orlitová I., Thuan T. X., Worseck G., Guseva N. G., 2016, *Astronomy & Astrophysics*, 591, L8
- Schaerer D., Marques-Chaves R., Barrufet L., Oesch P., Izotov Y. I., Naidu R., Guseva N. G., Brammer G., 2022, First look with JWST spectroscopy: Σz ~ 8 galaxies resemble local analogues, doi:10.48550/arXiv.2207.10034, <http://arxiv.org/abs/2207.10034>
- Senchyna P., et al., 2017, *Monthly Notices of the Royal Astronomical Society*, 472, 2608
- Shirazi M., Brinchmann J., 2012, *Monthly Notices of the Royal Astronomical Society*, 421, 1043
- Smit R., et al., 2014, *The Astrophysical Journal*, 784, 58
- Stark D. P., et al., 2017, *Monthly Notices of the Royal Astronomical Society*, 464, 469
- Stasinska G., 2007, in arXiv:0704.0348 [astro-ph]. Cambridge University Press, XVIII Canary Island Winterschool, <http://arxiv.org/abs/0704.0348>
- Storey P. J., Hummer D. G., 1995, *Monthly Notices of the Royal Astronomical Society*, 272, 41
- Storey P. J., Zeppen C. J., 2000, *Monthly Notices of the Royal Astronomical Society*, 312, 813
- Storey P. J., Sochi T., Badnell N. R., 2014, *Monthly Notices of the Royal Astronomical Society*, 441, 3028
- Tacchella S., et al., 2022, Technical report, JWST NIRC2+NIRSpec: Interstellar medium and stellar populations of young galaxies with rising star formation and evolving gas reservoirs, <https://ui.adsabs.harvard.edu/abs/2022arXiv220803281T>, <https://ui.adsabs.harvard.edu/abs/2022arXiv220803281T>
- Tang M., Stark D. P., Chevallard J., Charlot S., 2019, *Monthly Notices of the*

- Royal Astronomical Society, 489, 2572
- Tayal S. S., 2000, *The Astrophysical Journal*, 530, 1091
- Tayal S. S., 2007, *The Astrophysical Journal Supplement Series*, 171, 331
- Tayal S. S., 2011, *The Astrophysical Journal Supplement Series*, 195, 12
- Tayal S. S., Zatsarinny O., 2010, *The Astrophysical Journal Supplement Series*, 188, 32
- Terlevich R., Melnick J., Masegosa J., Moles M., Copetti M. V. F., 1991, *Astronomy and Astrophysics Supplement Series*, 91, 285
- Terlevich R., Silich S., Rosa-González D., Terlevich E., 2004, *Monthly Notices of the Royal Astronomical Society*, 348, 1191
- Trump J. R., et al., 2022, The Physical Conditions of Emission-Line Galaxies at Cosmic Dawn from JWST/NIRSpec Spectroscopy in the SMACS 0723 Early Release Observations, doi:10.48550/arXiv.2207.12388, <http://arxiv.org/abs/2207.12388>
- Vilchez J. M., Pagel B. E. J., 1988, *Monthly Notices of the Royal Astronomical Society*, 231, 257
- Virtanen P., et al., 2020, *Nature Methods*, 17, 261
- Weilbacher P. M., Streicher O., Urrutia T., Jarno A., Pécontal-Rousset A., Bacon R., Böhm P., 2012, in *Software and Cyberinfrastructure for Astronomy II*. SPIE, pp 102–110, doi:10.1117/12.925114, <https://www.spiedigitallibrary.org/conference-proceedings-of-spie/8451/84510B/Design-and-capabilities-of-the-MUSE-data-reduction-software-and-10.1117/12.925114.full>
- Wiese W. L., Fuhr J. R., Deters T. M., 1996, Atomic transition probabilities of carbon, nitrogen, and oxygen : a critical data compilation. Springer
- Worthey G., 1994, *The Astrophysical Journal Supplement Series*, 95, 107
- Yang C., He Z., Yu W., 2009, *BMC Bioinformatics*, 10, 4
- Yang H., et al., 2017, *The Astrophysical Journal*, 844, 171
- Zeippen C. J., 1982, *Monthly Notices of the Royal Astronomical Society*, 198, 111
- Zwicky F., Kowal C. T., 1968, Catalogue of Galaxies and of Clusters of Galaxies. Astronomy and Astrophysics Library Vol. 6, Caltech, Pasadena, CA, <https://resolver.caltech.edu/CaltechAUTHORS:20130417-142619262>
- van Zee L., 2000, *The Astronomical Journal*, 119, 2757
- van Zee L., 2001, *The Astronomical Journal*, 121, 2003
- van Zee L., Haynes M., 2005, *The Astrophysical Journal*, 636

APPENDIX A: SOME EXTRA MATERIAL

If you want to present additional material which would interrupt the flow of the main paper, it can be placed in an Appendix which appears after the list of references.

This paper has been typeset from a $\text{\TeX}/\text{\LaTeX}$ file prepared by the author.

Table A1. Atomic data references for the emission lines considered in the chemical analysis.

Ion	Atomic data	
<i>H</i>	Storey & Hummer (1995)	
<i>He</i>	Porter et al. (2012)	
<i>He</i> ⁺	Storey & Hummer (1995)	
Ion	Collision Strengths	Transition probabilities
<i>O</i> ⁺	Pradhan et al. (2006); Tayal (2007)	Zeippen (1982); Wiese et al. (1996)
<i>S</i> ⁺	Tayal & Zatsarinny (2010)	Podobedova et al. (2009)
<i>O</i> ⁺²	Storey et al. (2014)	Storey & Zeippen (2000); Wiese et al. (1996)
<i>N</i> ⁺	Tayal (2011)	Wiese et al. (1996); Galavís et al. (1997)
<i>S</i> ⁺²	Hudson et al. (2012)	Podobedova et al. (2009)
<i>S</i> ⁺³	Tayal (2000)	Dufton et al. (1982); Johnson et al. (1986)
<i>Ar</i> ⁺²	Galavís et al. (1995)	Kaufman & Sugar (1986); Galavís et al. (1995)
<i>Ar</i> ⁺³	Ramsbottom & Bell (1997)	Mendoza & Zeippen (1982)

Table A2. Priors and likelihood distributions in our model. The term X^{i+} includes all the ionic metal abundances: Ar^{2+} , Ar^{3+} , Cl^{3+} , Fe^{3+} , O^+ , O^{2+} , Ne^{3+} , N^+ , S^+ , S^{2+} , y^+ and y^{2+} . The helium abundances are defined in logarithmic scale, while the metals are defined using a $12+\log(X^{i+})$ notation.

Parameter	Prior distribution
T_{low}	$Normal(\mu = 15000\text{ K}, \sigma = 5000\text{ K})$
T_{high}	$Normal(\mu = 15000\text{ K}, \sigma = 5000\text{ K})$
n_e	$Half\ Cauchy(\mu = 2.0, \sigma = 0)$
$c(H\beta)$	$Half\ Cauchy(\mu = 2.0, \sigma = 0)$
X^{i+}	$Normal(\mu = 5, \sigma = 5)$
y^+	$Normal(\mu = 0, \sigma = 3)$
y^{2+}	$Normal(\mu = 0, \sigma = 3)$
T_{eff}	$Uniform(min = 30000\text{ K}, max = 90000\text{ K})$
$\log(U)$	$Uniform(min = -4.0, max = -1.0)$
Parameter	Likelihood distribution
$\frac{F_{X^{i+}, \lambda}}{F_{H\beta}}$	$Normal(\mu = \frac{F_{X^{i+}, \lambda, obs}}{F_{H\beta}}, \sigma = \frac{\sigma_{X^{i+}, \lambda, obs}}{F_{H\beta}})$